

NEUTRINO TRANSPORT WITH MONTE CARLO METHOD: II. QUANTUM KINETIC EQUATIONS

CHINAMI KATO,^{1,2} HIROKI NAGAKURA,³ AND TAIKI MORINAGA⁴

¹*Department of Aerospace Engineering, Tohoku University, 6-6-01 Aramaki-Aza-Aoba, Aoba-ku, Sendai 980-8579, Japan*

²*Department of Science and Technology, Tokyo University of Science, 2641 Yamazaki, Noda-shi, Chiba Prefecture 278-8510, Japan*

³*Department of Astrophysical Sciences, Princeton University, Princeton, NJ 08544*

⁴*Graduate School of Advanced Science and Engineering, Waseda University, 3-4-1 Okubo, Shinjuku, Tokyo 169-8555, Japan*

(Received; Revised; Accepted)

Submitted to ApJS

ABSTRACT

Neutrinos have a unique quantum feature as flavor conversions. Recent studies suggested that collective neutrino oscillations play important roles in high-energy astrophysical phenomena. Quantum kinetic equation (QKE) is capable of describing the neutrino flavor conversion, transport and matter collision self-consistently. However, we have experienced many technical difficulties in their numerical implementation. In this paper, we present a new QKE solver based on Monte Carlo (MC) approach. This is an upgraded version of our classical MC neutrino transport solver; in essence, a flavor degree of freedom including mixing state is added into each MC particle. This extension requires updating numerical treatments of collision terms, in particular for scattering processes. We deal with the technical problem by generating a new MC particle at each scattering event. To reduce statistical noise inherent in MC methods, we develop the effective mean free path method. This suppresses a sudden change of flavor state due to collisions without increasing the number of MC particles. We present a suite of code tests to validate these new modules with comparing to the results reported in previous studies. Our QKE-MC solver is developed with fundamentally different philosophy and design from other deterministic- and mesh methods, suggesting that it will be complementary to others, and potentially provide new insights into physical processes of neutrino dynamics.

Keywords: supernova:general — neutrinos —

1. INTRODUCTION

In hot and dense media, neutrinos have important roles as effective carriers of energy and lepton-number. During the advanced stages of massive star evolution ($M \gtrsim 10M_\odot$), neutrino cooling dictates the thermal evolution of the stellar core (Farag et al. 2020; Odrzywolek & Heger 2010). In the subsequent core-collapse supernova (CCSN), neutrinos are produced abundantly via various weak interaction processes. The neutrino transport and their matter interactions may be central to the explosion mechanism (Janka 2012; Kotake et al. 2012; Foglizzo et al. 2015; Mirizzi et al. 2016; Müller 2019, 2020; Burrows & Vartanyan 2021), and of nucleosynthesis of heavy elements (Martínez-Pinedo et al. 2014; Harris et al. 2017; Wanajo et al. 2018; Sieverding et al. 2020; Witt et al. 2021). Regardless of the detailed explosion mechanism, the emitted neutrinos from Galactic events are observable signals by current and future-planned terrestrial detectors. The direct detection of neutrinos from these nearby CCSNe will provide high statistics neutrino data, that will shed light on the inner dynamics of CCSN (Horiuchi & Kneller 2018; Gallo Rosso et al. 2018; Suwa et al. 2019; Nagakura et al. 2021; Nagakura 2021; Li et al. 2021; Mori et al. 2021). The remnant of binary neutron star merger (BNSM) is another exciting production site of neutrinos, that has received huge interest with the dawn of multi-messenger astrophysics (Abbott et al. 2017). Although neutrino dynamics is a key ingredient to account for the time evolution of the system, the detailed flavor-dependent features of energy spectrum and angular distributions of neutrinos are still uncertain. Accurate treatments of neutrino transport and neutrino-matter interactions are indispensable towards understanding of the global dynamics, ejecta composition and observable signals including kilonova transients (Sekiguchi et al. 2015; Thielemann et al. 2017; Siegel & Metzger 2017; Radice et al. 2018; Miller et al. 2019; Kawaguchi et al. 2021).

There is growing experimental evidence that neutrinos' flavor states oscillate from one to another during the propagation, known as neutrino oscillation. The flavor mixing is attributed to the fact that neutrinos are massive particles, and that their mass- and flavor eigenstates are not identical each other. In a vacuum, the flavor conversion is dictated by the difference of eigenvalues of the mass eigenstates (i.e., the mass difference of neutrinos), and non-zero mixing angles. Accurate determination of these oscillation parameters is the major challenge in experimental physics, that has made remarkable progress over the past decades (Abe et al. 2014; Adamson et al. 2014; T2K Collaboration & Abe 2014;

Abe et al. 2018a,b; Aartsen et al. 2018; Acero et al. 2019; Esteban et al. 2020).

Neutrinos experience refractive effects when they propagate in matter. This changes the dispersion relation of neutrinos, implying that flavor conversions are altered. The matter effect dominates over the vacuum oscillation in CCSNe and remnants of BNSM. This may induce strong flavor mixing at the resonance MSW matter density (Wolfenstein 1978). Another important consequence of the matter effect is that the mixing angles between flavor- and effective mass eigenstates are substantially reduced at a high density region, indicating that the flavor conversion is strongly suppressed. This is a rationale behind the assumption that no flavor mixing occur in a CCSN/BNSM core (e.g., Fuller et al. 1987; Dighe & Smirnov 2000); indeed, almost every numerical simulation has been carried out with the assumption.

However, refractive effects by neutrino-self interactions potentially induce strong flavor conversion, also known as collective neutrino oscillations (Samuel 1993; Sigl & Raffelt 1993; Sigl 1995; Sawyer 2005). They are genuinely a non-linear phenomenon with large off-diagonal components of the Hamiltonian potential in the flavor-basis, suggesting that the flavor conversion is qualitatively different from that induced by the vacuum and matter potentials. The collective oscillation involves two distinct modes: fast- and slow flavor conversions. The time scales of these flavor conversions are very short, in particular for the fast mode; the oscillation frequency increases proportionally to the neutrino number density. Although the growth rate of the slow mode is relatively mild, various interesting phenomena have been found, for instances, spectral swaps/splits, bipolar and synchronized oscillations, although the occurrence of these phenomena in CCSN and BNSM environments are still being debated (Duan et al. 2006a,b; Dasgupta et al. 2009; Tian et al. 2017; Martin et al. 2020a).

In the last several years, there has been significant progress of our theoretical understanding of collective neutrino oscillations. Some of the progress are owed to the linear stability analysis that provides not only insights into characteristics of collective neutrino oscillations but also criteria to assess the onset of flavor conversions (Dasgupta et al. 2017; Nagakura et al. 2019; Delfan Azari et al. 2019; Abbar et al. 2020; Morinaga et al. 2020; Delfan Azari et al. 2020). Regarding the fast mode, electron neutrino lepton number crossings (ELN crossings) in angular distributions are associated with the instability (Morinaga 2021). The recent studies suggested that ELN crossings have been frequently observed in the neutrino data of CCSN and BNSM simulations (Tamborra et al.

2017; Wu & Tamborra 2017; Dasgupta et al. 2018; Glas et al. 2020; Abbar 2020; Capozzi et al. 2020; Abbar 2021; Abbar et al. 2021), that increases the possibility of occurrence of fast flavor conversion in real CCSN/BNSM environments. Concerning the slow mode, some recent studies have demonstrated that this type of flavor oscillation affects observational consequences of CCSNe such as nucleosynthesis and neutrino signals (Chakraborty et al. 2010; Zaizen et al. 2018; Sasaki et al. 2017; Wu et al. 2017; George et al. 2020). These results motivate more detailed studies of collective neutrino oscillations.

Aside from a flavor mixing, neutrinos experience absorption and momentum-exchanged scattering¹ during the propagation in medium. The macroscopic properties of neutrino radiation field in CCSN and BNSM strongly hinge on these collision term. They also affect the dynamics of collective neutrino oscillations; for instances, both fast and slow modes may be triggered by neutrino scatterings with nucleons or nuclei (Cherry et al. 2013, 2020; Morinaga et al. 2020; Zaizen et al. 2020); the characteristics of flavor conversions may be altered by these scatterings (Capozzi et al. 2019; Johns et al. 2020; Shalgar & Tamborra 2021a,b; Martin et al. 2021); Johns (2021) suggested very recently that a new type of instability, collisional flavor instability, appears due to collision terms. Hence, the coupling between collective neutrino oscillations and collision terms is currently of great interest. On the other hand, time scales of neutrino-matter collisions are usually longer than that of neutrino oscillations, indicating that the investigation of the interplay to neutrino-matter collisions should inevitably be in non-linear phase of collective oscillations. The direct numerical simulation is, hence, the most useful approach for the investigation.

The consistent treatment of neutrino transport, flavor conversion and neutrino-matter collisions requires the quantum kinetic description of the neutrino-radiation field. The quantum kinetic equation (QKE) provides the basic equation, that can be concisely written in the mean-field approximation (see also Eq. 1). However, the direct numerical simulation is not an easy task, but rather a grand challenge in computational physics. This is mainly attributed to the large disparity of time- and spatial scales between flavor conversions and global (macroscopic) system. Recent studies in Johns et al. (2020); Richers et al. (2021) also found that fast flavor conversions generally involve cascade phenomena,

in which fast flavor conversions trigger the energy exchange between large- to small scales. This suggests that small scale structures of both spatial- and momentum spaces need to be resolved, posing another challenge in numerical simulations. For these reasons, the currently feasible approach is either local simulations (Abbar & Volpe 2019; Richers et al. 2019; Martin et al. 2020b; Shalgar & Tamborra 2021a; Richers et al. 2021; Martin et al. 2021; Zaizen & Morinaga 2021) or large-scale simulations with employing crude approximations and simplifications (see, e.g., Duan et al. 2006a; Dasgupta & Dighe 2008; Cherry et al. 2012; Zaizen et al. 2018; Stapleford et al. 2020; Li et al. 2021).

Regarding the methodologies, there are mainly two options: deterministic- and probabilistic approaches. The former has been popular in QKE neutrino transport. This may be because the numerical technique can be simply extended from classical radiation transport; indeed, it is a good compatibility with finite volume methods (but see a PIC method in Richers et al. (2021)). On the other hand, there are no previous work that employ the probabilistic way in QKE neutrino transport. The main reason of the absence of demonstration is that probabilistic treatments are not necessary in QKE neutrino transport, unless the collision term is taken into account. As already mentioned, however, there is a growing interest in interplay between flavor conversions and collision terms, indicating that the detailed investigation of the coupling system will be made more vigorously in future. It should also be mentioned that, since all numerical simulations involve a certain level of approximation, it is necessary to assess the reliability of their results. Independent numerical approach will help the assessment, and provide confidence in the accuracy of each result. In fact, such collaborative code-comparison projects can be seen in classical neutrino transport (Richers et al. 2017; O'Connor et al. 2018).

In this paper, we present a new QKE neutrino transport solver based on a Monte Carlo (MC) method, which is a representative probabilistic approach. This QKE-MC code is an extension version of our classical MC neutrino transport one (Kato et al. 2020), in which the neutrino transport with various weak processes are well tested in the context of CCSN simulations. On the other hand, there is a non-trivial issue: how the quantum kinetic states can be handled in the particle method. Addressing this issue is one of the focuses in this paper. We develop new modules to reduce the statistical noise inherent to the MC approach, and to increase the computational efficiency. After presenting the numerical implementation, we demonstrate a suite of code

¹ We note that the term "momentum-exchanged scattering" is used to distinguish from the forward scattering generating neutrino refraction.

tests including fast flavor conversions with momentum-exchanged scatterings to test the capability of these new modules.

This paper is organized as follows. We start with providing an overview of the QKE for neutrino transport in Sec. 2. The essential methodologies in our QKE-MC solver are described in Sec. 3. Before entering into the detail of code tests, we describe the basic assumption in Sec. 4. From Secs. 5 to 7, we present code tests for vacuum, matter and collective neutrino oscillations, respectively. Other tests regarding QKE with scatterings are demonstrated in Sec. 8. We conclude the paper with a summary and discussions in Section 9. Throughout this paper, we use the metric signature of $(-+++)$. Unless otherwise stated, Greek subscripts denote the spacetime components, and we work in units with $c = \hbar = 1$, where c and \hbar denote the speed of light and reduced Planck constant, respectively.

2. BASIC EQUATION

The QKE for neutrino transport can be written as (see also Sigl & Raffelt 1993; Volpe 2015),

$$\begin{aligned} & i \left(p^\alpha \frac{\partial \rho}{\partial x^\alpha} \Big|_{p^i} - \Gamma_{\alpha\beta}^i p^\alpha p^\beta \frac{\partial \rho}{\partial p^i} \Big|_{x^\mu} \right) \\ &= (-p^\mu \zeta_\mu) [H_{\text{vac}} + H_{\text{mat}} + H_{\nu\nu}, \rho] + C, \\ & i \left(p^\alpha \frac{\partial \bar{\rho}}{\partial x^\alpha} \Big|_{p^i} - \Gamma_{\alpha\beta}^i p^\alpha p^\beta \frac{\partial \bar{\rho}}{\partial p^i} \Big|_{x^\mu} \right) \\ &= (-p^\mu \zeta_\mu) [H_{\text{vac}}^* - H_{\text{mat}}^* - H_{\nu\nu}, \bar{\rho}] + \bar{C}, \end{aligned} \quad (1)$$

where ρ ($\bar{\rho}$) is the density matrix for neutrinos (anti-neutrinos); x^μ denotes the space-time coordinate; p^μ denotes the four-momentum of neutrinos; C (\bar{C}) is the collision term for neutrinos (anti-neutrinos); Γ is the Christoffel symbols; ζ^μ denotes the unit vector normal to the spatial hypersurface of $t = \text{const}$, where t is the laboratory time. In the expression, Hamiltonian operators are measured in the laboratory frame². Each potential can be given as

$$\begin{aligned} H_{\text{vac}} &= U \frac{M^2}{2E_\nu} U^\dagger, \\ H_{\text{mat}} &= \sqrt{2} G_F \frac{p_\mu}{E_\nu} \text{diag}[j_l^\mu - \bar{j}_l^\mu], \\ H_{\nu\nu} &= \sqrt{2} G_F \int dV_{p'} \frac{p^\mu p'_\mu}{E_\nu E'_\nu} (\rho' - \bar{\rho}'^*). \end{aligned} \quad (2)$$

In the expression, M^2 can be written as $M_{ij}^2 = m_a^2 \delta_{ij}$ (the index a specifies the mass eigenstate of neutrinos)

² We note that it can be measured with arbitrary time. In this case, we replace $(-p^\mu \zeta_\mu)$ by $(-p^\mu \zeta'_\mu)$ in Eq. 1, where ζ'_μ denotes the arbitrary timelike vector.

in the relativistic limit, where m_a denote the rest-mass of ν_a . $E_\nu = -p^\mu \zeta_\mu$ represents the energy of neutrinos measured by an observer of ζ_μ . U is the unitary matrix describing the mixing between flavor and mass bases. G_F is the Fermi coupling constant. j_l^μ represents the number current of charged-leptons, which can be written as $j_l^\mu = n_l u_l^\mu$, where n_l and u_l^μ denotes the number density (measured at each lepton's rest frame) and four-velocity of each charged-leptons, respectively. dV_p denotes the momentum volume element for neutrino momentum space, which can be written as

$$dV_p = \frac{1}{(2\pi)^3} d\Omega d\left(\frac{E_\nu^3}{3}\right), \quad (3)$$

where $d\Omega$ denotes the solid angle of neutrinos measured in ζ_μ observer³.

3. NUMERICAL IMPLEMENTATIONS

Many modules in our QKE-MC solver are imported from classical one (Kato et al. 2020). However, the flavor states in MC particles are no longer constant during the flight due to flavor conversions. A possible solution is that a flavor degree of freedom is added in each MC particle. This change also requires an update of treatments for collision terms. In this section, we describe our new ideas of the formulation and numerical techniques for them.

3.1. Transport and oscillation

Each MC particle of position and momentum state follows the geodesic equation during propagation,

$$\begin{aligned} \frac{dx^\mu}{d\lambda} &= p^\mu, \\ \frac{dp^\mu}{d\lambda} - \Gamma_{\alpha\beta}^\mu p^\alpha p^\beta &= 0, \end{aligned} \quad (4)$$

where λ denotes the affine parameter for a trajectory of each particle. We assume neutrinos as massless particles, i.e., Eq. 4 is null geodesics. It is a reasonable assumption for CCSN and BNSM system, since the typical energy of neutrinos are above MeV and it is much larger than the rest mass of neutrinos ($\lesssim 0.1$ eV) (Aker et al. 2019). We note that neutrinos are treated as massive particles in the evolution of flavor state (see below).

Different from conventional MC neutrino transport, the flavor degree of freedom is embedded in each MC particle, that allows us to treat the neutrino flavor conversion self-consistently. More specifically, we define the

³ We note that ζ_μ can be replaced any time-like unit vector. This depends on the choice of tetrad basis to describe the momentum space of neutrinos (see e.g., Shibata et al. 2014, for more detail).

particle-matrix, q , on each MC particle. The matrix structure of q is the same as that of density matrix (ρ), i.e., $N_f \times N_f$ matrix (N_f denotes the number of flavor). The matrix element represents the number of particles in the flavor basis, i.e., this is a natural extension from "sample particles" used in classical MC method. The density matrix (ρ) at each time can be computed from q as

$$\begin{aligned} \rho(\mathbf{x}, \mathbf{p}) &= \lim_{\Delta V_x \rightarrow 0} \lim_{\Delta V_p \rightarrow 0} \frac{1}{\Delta V_x \Delta V_p} \\ &\times \sum_s q_s \int_{\mathbf{x}-0.5\Delta\mathbf{x}}^{\mathbf{x}+0.5\Delta\mathbf{x}} \int_{\mathbf{p}-0.5\Delta\mathbf{p}}^{\mathbf{p}+0.5\Delta\mathbf{p}} dV'_x dV'_p \\ &\times \delta^3(\mathbf{x}' - \mathbf{x}_s(t)) \\ &\times (2\pi)^3 \delta^3(\mathbf{p}' - \mathbf{p}_s(t)), \end{aligned} \quad (5)$$

where s denotes the index of a MC particle, and $\bar{\rho}$ (anti-neutrinos) can be computed by replacing $q \rightarrow \bar{q}$. In the expression, x_s and p_s are the spatial position and momentum of s -th QKE-MC particle, respectively; dV_x denotes a spatial three-dimensional volume element,

$$dV_x = \sqrt{-g} dx_1 dx_2 dx_3, \quad (6)$$

where g denotes the determinant of the space-time metric.

In practice, ρ is computed by setting finite but small values of ΔV_x and ΔV_p in Eq. 5. Here we take the on-shell condition for neutrinos. The number density of neutrinos (measured in the laboratory frame) can be computed through ρ ,

$$n_{ij} = \int \rho_{ij} dV'_p, \quad (7)$$

where i and j specify the flavor state. The anti-neutrino counterpart can be given by replacing $\rho \rightarrow \bar{\rho}$.

We evolve q and \bar{q} as

$$\begin{aligned} i \frac{dq_s}{d\lambda} &= (-p^\mu n_\mu) [H_{\text{vac}} + H_{\text{mat}} + H_{\nu\nu}, q_s], \\ i \frac{d\bar{q}_s}{d\lambda} &= (-p^\mu n_\mu) [H_{\text{vac}}^* - H_{\text{mat}}^* - H_{\nu\nu}^*, \bar{q}_s], \end{aligned} \quad (8)$$

where $d/d\lambda$ in Eq. 8 is an ordinary differentiation, which is solved with forth-order explicit Runge-Kutta method. We note that the self-interaction potential, $H_{\nu\nu}$, can be computed from q and \bar{q} by using Eqs. 2 and 5.

3.2. Collision term

The implementation of collision terms is well established in classical MC method, and its extension to QKE is straightforward. Below, we first describe the essence of the extension.

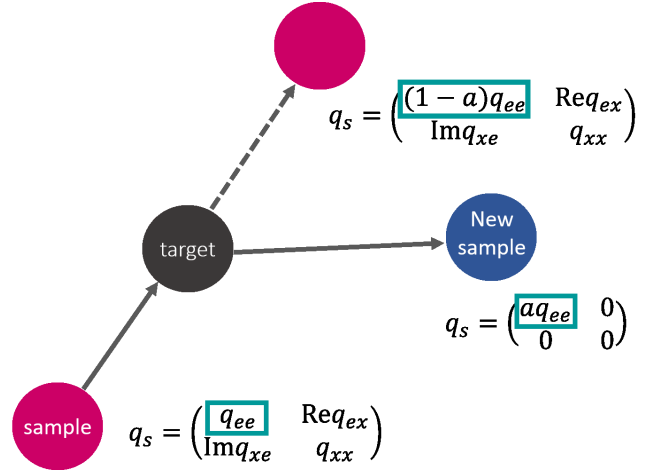


Figure 1. The schematic picture illustrating our numerical treatments of scattering process. As an example, we display the case that ν_e (ee component of q) experiences scatterings. We note that a corresponds to a control parameter relevant to effective mean free path (EMFP) method. See text for more detail.

Let us start with emission processes. Although the neutrino matter interaction needs to be changed with the extension of QKE (Vlasenko et al. 2014; Blaschke & Cirigliano 2016), the implementation is the same as that used in classical MC transport. The blocking factor can also be taken into account by the same prescription used in our classical MC method. We generate new MC particles with specifying the neutrino energy and flight direction. Following the neutrino emissivity, we insert the value of neutrino number of production into each matrix element of q_s (and \bar{q}_s) of newly generated MC particles.

For absorption process, we probabilistically determine the absorption length, the distance to a position where the neutrinos experience absorption; the procedure is exactly the same as that used in our classical MC transport. We note, however, that the length can not be assigned into each MC particle, since the reaction rate in general varies with the neutrino flavor. Therefore, it is assigned to each flavor state of MC particles. MC particles are evolved following the geodesic equation until the travel distance reaches the absorption length. At the absorption point, the corresponding matrix element of q set to be zero. If q becomes completely null due to the absorption, we exclude the MC particle from our simulations.

The scattering process can be handled as the similar procedure as that used in neutrino absorptions. The scattering length, a distance to a point where the MC particle scatters with matter, is determined probabilistically. Since it is varied with neutrino flavor state, the

scattering length is assigned to each matrix element of MC particle. At the scattering point, we generate a new MC particle, in which the neutrino energy and flight direction is chosen so as to coincide with the scattered neutrinos⁴; i.e., it plays a role of the particle after the scattering (see Fig. 1). The matrix element of q in the new MC particle is copied from that in the original particle, meanwhile we set zero in the matrix component of q of the original MC particle (but see below for a corrected treatment to reduce the statistical noise). It should be emphasized that this prescription guarantees the exact conservation of neutrino numbers.

Although these treatments are capable of providing accurate solutions in principle, the statistical noise inherent in MC methods is a concern. It would affect self-interaction potentials, and then unphysical flavor oscillations may be induced. Indeed, it potentially generate artificial ELN crossings, that would kick in artificial fast neutrino flavor conversions. It should be stressed that the problem is unavoidable as long as the number of MC particle is finite⁵, indicating that the special treatment is mandatory.

To overcome the difficulty, we adopt a smoothing prescription in evaluating the self-interaction potential. Similar as mesh methods, we discretize the 6-dimensional phase space, and compute ρ on each mesh by using Eq. 5. The momentum integral of neutrinos in self-interaction potential is calculated by using ρ . More specifically, we adopt the values of energy and flight directions at the cell center value of the momentum space grid in computations of the self-interaction potential. Although the prescription smears out a small scale structure of neutrino momentum space, the statistical noise can be controlled by changing the mesh resolution. This should be set appropriately depending on the problem.

We develop another prescription of collision terms to further reduce the statistical noise, namely effective mean free path method (hereafter we refer to it as EMFP method). In general, large statistical noise potentially appears when the MC particle experiences an absorption or scattering with matter. This is attributed to the fact that a MC particle represents a bundle of neutrinos, and that the physical states of all neutrinos change suddenly at each absorption/scattering point. Although the most straightforward way to reduce the noise is to

increase the number of MC particles or to run many simulations for the increase of statistics, we propose another way to address the issue; the essence is as follows. We introduce a control parameter, a ($0 \leq a \leq 1$), that determines the rate of change in each MC particle by neutrino matter interactions. Let us provide an example how we use a for scattering processes. At the scattering point, $a \times q_{ij}$ (where i, j specify the flavor of scattered neutrinos) is transferred from the original MC particle to the new one (see Fig. 1), i.e., the change of q is softened by a . To compensate this effect, we reduce the scattering length by the same factor of a . As we show in Sec. 8.1, this does not affect the physical solution of QKE system. The merit of this prescription is that the statistical noise can be reduced without pressing memory capacity in simulations.

One may wonder if the above prescription causes increasing numerical costs and makes the simulation unfeasible. In fact, the number of scattering events increases proportional to $1/a$. It should be noted, however, that this problem is under control; indeed $a = 1$ recovers the original treatment. Importantly, this prescription is suited for problems of our interest: interplay between collision terms and collective neutrino oscillations. The reason is as follows. The time scale of collective neutrino oscillation is usually much shorter than that of neutrino-matter collisions, indicating that the numerical cost is dominated by transport- and oscillation terms. Indeed, for the case with $a = 1$, almost every MC particle does not interact with matter during each time step (Δt) of simulations. By introducing a , we can manage the balance of computational time among different terms. As a result, we successfully increase the statistics without both pressing memories and computational cost.

We make another important remark regarding the number of MC particles. In our treatments of collision term, the number of MC particles tends to increase with time, since new MC particles are generated in not only emission but also scattering processes. We address this issue by the following prescription. When the particle number almost exceeds the limit of computational resources, we combine adjacent MC particles so that the number, energy, and moment of neutrinos are conserved.

⁴ These momentum space values, i.e., p^μ , can be determined through the same probabilistic way used in our classical MC method (see Kato et al. (2020)).

⁵ In any particle-based methods, we can always take an infinitesimal solid angle so that the number of particle is zero, indicating that artificial ELN crossings are ubiquitous at the small scale.

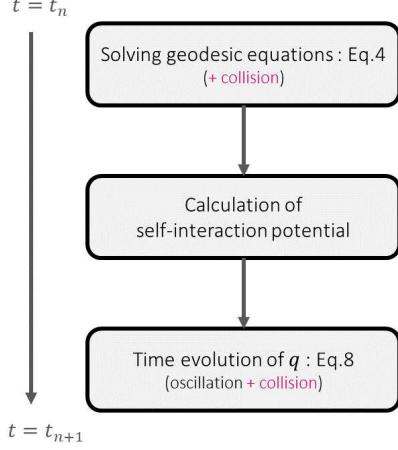


Figure 2. The flow chart for our QKE-MC solver. We highlight the parts associated with neutrino-matter interactions as purple color.

Although the prescription violates the causality, this effect is expected to be minor⁶.

3.3. Flow chart

To facilitate readers' understanding, we provide a flow chart of our QKE-MC solver in Fig. 2. It summarizes the overall procedure for the time evolution of $t = t_n$ to t_{n+1} . We first evolve the MC particles by solving Eq. 4. If the scattering and absorption processes are included, we change the flight direction and energy of neutrinos during the time step. The spatial transport of generated MC particles associated with scatterings (see Sec. 3.2) are also handled there. It should be mentioned that we do not evolve q of each MC particle at this step.

As the next step, we compute the self-interaction potential from MC particles. As mentioned in Sec. 3.2, we employ a smoothing prescription to evaluate it if collision terms are taken into account. We then evolve q and \bar{q} by solving Eq. 8.

There are two important remarks in the above procedure. First, we treat the time evolution of q as a similar procedure of operating-splitting method; in which neutrino oscillations and collision terms are handled separately. As we have described in Sec. 3.2, matrix elements of scattered MC particles needs to be corrected, and the new generated one takes over them (see also Fig. 1). This computation is done after solving Eq. 8, i.e., com-

pleting the transport- and oscillation processes. As long as Δt is small enough to resolve the system, the artifact due to the prescription is negligible. Second, the actual procedure of our QKE-MC solver is a bit more complicated than that described above. This is because the high-order time integration (fourth-order Runge-Kutta method) is implemented in our QKE-MC. We update the self-interaction potential at each sub-step. We note that the high-order precision is necessary only for solving Eq. 8, i.e., to determine the evolution of neutrino flavor conversions. Except for the computation of flavor conversion, we adopt the Eulerian integration in their time integration.

4. BASIC ASSUMPTIONS IN CODE TESTS

Although our QKE-MC solver is capable of handling the problems with arbitrary number of neutrino flavors, we assume a two flavor system throughout the code tests. In the approximation, the density matrix has four independent components that can be written as,

$$\rho = \begin{pmatrix} \rho_{ee} & \rho_{ex} \\ \rho_{ex}^* & \rho_{xx} \end{pmatrix}, \quad \bar{\rho} = \begin{pmatrix} \bar{\rho}_{ee} & \bar{\rho}_{ex} \\ \bar{\rho}_{ex}^* & \bar{\rho}_{xx} \end{pmatrix}. \quad (9)$$

In the two flavor system, the expression with the polarization vector \mathbf{P} and $\bar{\mathbf{P}}$ in the flavor space is useful. It is defined as,

$$\rho = \frac{1}{2} (\rho_{ee} + \rho_{xx}) I + \frac{1}{2} \mathbf{P} \cdot \boldsymbol{\sigma},$$

$$\bar{\rho} = \frac{1}{2} (\bar{\rho}_{ee} + \bar{\rho}_{xx}) I + \frac{1}{2} \bar{\mathbf{P}} \cdot \boldsymbol{\sigma}^*, \quad (10)$$

where σ and I denotes the Pauli matrix and Unit matrix. The component of polarization vector can be written as,

$$\mathbf{P} = \begin{pmatrix} 2\text{Re}\rho_{ex} \\ -2\text{Im}\rho_{ex} \\ \rho_{ee} - \rho_{xx} \end{pmatrix}, \quad \bar{\mathbf{P}} = \begin{pmatrix} 2\text{Re}\bar{\rho}_{ex} \\ 2\text{Im}\bar{\rho}_{ex} \\ \bar{\rho}_{ee} - \bar{\rho}_{xx} \end{pmatrix}. \quad (11)$$

Using the polarization vectors, Eq. 1 can be written as Bloch-type equations:

$$\frac{D}{d\lambda} \mathbf{P} = \left[\omega \mathbf{B} + \sqrt{2} G_F (n_e - \bar{n}_e - n_x + \bar{n}_x) \mathbf{u} \right. \\ \left. + \sqrt{2} G_F \int dV_{p'} \frac{p^\mu p'_\mu}{E_\nu E'_\nu} (\mathbf{P}' - \bar{\mathbf{P}}') \right] \times \mathbf{P},$$

$$\frac{D}{d\lambda} \bar{\mathbf{P}} = \left[-\omega \mathbf{B} + \sqrt{2} G_F (n_e - \bar{n}_e - n_x + \bar{n}_x) \mathbf{u} \right. \\ \left. + \sqrt{2} G_F \int dV_{p'} \frac{p^\mu p'_\mu}{E_\nu E'_\nu} (\mathbf{P}' - \bar{\mathbf{P}}') \right] \times \bar{\mathbf{P}}, \quad (12)$$

where θ is the angle between the propagation directions of two neutrinos and $\omega \equiv \Delta m^2 / 2E_\nu$ is the vacuum

⁶ Regarding the causality, the computation of self-interaction potential is also an issue, since it is computed by collecting MC particles located at different spatial locations. However, the error can be estimated by the convergence study; indeed, the solution approaches to the real by increasing the number of MC particles and decreasing the phase space volume in the computation of ρ .

oscillation frequency with the mass difference $\Delta m^2 \equiv m_2^2 - m_1^2$. In the expression, we use the following expressions for Hamiltonian potentials,

$$\begin{aligned} H_{\text{vac}} &= \frac{1}{2} \omega \mathbf{B} \cdot \boldsymbol{\sigma}, \\ H_{\text{mat}} &= \frac{\sqrt{2}}{2} G_F (n_e - \bar{n}_e - n_x + \bar{n}_x) \mathbf{u} \cdot \boldsymbol{\sigma}, \\ H_{\nu\nu} &= \frac{\sqrt{2}}{2} G_F \int dV_{p'} \frac{p^\mu p'_\mu}{E_\nu E'_\nu} (\mathbf{P}' - \bar{\mathbf{P}}') \cdot \boldsymbol{\sigma}, \end{aligned} \quad (13)$$

with $\mathbf{u} = (0, 0, 1)$ and $\mathbf{B} = (\sin 2\theta_0, 0, -\cos 2\theta_0)$. θ_0 denotes the mixing angle. In this expression, we subtract the trace part, since they do not affect flavor conversions.

In the following code tests, we take the flat space-time. We also assume that the matter distribution is static and homogeneous. It should be mentioned that neutrino distributions are assumed to be homogeneous throughout our code tests. More detailed tests and scientific simulations including neutrino transport under inhomogeneous backgrounds are postponed to future work.

5. VACUUM OSCILLATIONS

We start with tests of vacuum oscillations. By virtue of the linear system, we can solve the time evolution of ρ analytically. They can be written in the flavor-basis as,

$$\begin{aligned} \rho_{ee} &= \left[1 - \sin^2 2\theta_0 \sin^2 \frac{\omega t}{2} \right] \rho_{ee}^0 \\ &+ \sin^2 2\theta_0 \sin^2 \frac{\omega t}{2} \rho_{xx}^0 \\ &- 2 \cos 2\theta_0 \sin 2\theta_0 \sin^2 \frac{\omega t}{2} \text{Re} \rho_{ex}^0 \\ &- \sin 2\theta_0 \sin \omega t \text{Im} \rho_{ex}^0, \end{aligned} \quad (14)$$

$$\begin{aligned} \rho_{xx} &= \sin^2 2\theta_0 \sin^2 \frac{\omega t}{2} \rho_{ee}^0 \\ &+ \left[1 - \sin^2 2\theta_0 \sin^2 \frac{\omega t}{2} \right] \rho_{xx}^0 \\ &+ 2 \cos 2\theta_0 \sin 2\theta_0 \sin^2 \frac{\omega t}{2} \text{Re} \rho_{ex}^0 \\ &+ \sin 2\theta_0 \sin \omega t \text{Im} \rho_{ex}^0, \end{aligned} \quad (15)$$

$$\begin{aligned} \text{Re} \rho_{ex} &= \cos 2\theta_0 \sin 2\theta_0 \sin^2 \frac{\omega t}{2} (\rho_{xx}^0 - \rho_{ee}^0) \\ &+ \left[1 - 2 \cos^2 2\theta_0 \sin^2 \frac{\omega t}{2} \right] \text{Re} \rho_{ex}^0 \\ &- \cos 2\theta_0 \sin \omega t \text{Im} \rho_{ex}^0, \end{aligned} \quad (16)$$

$$\begin{aligned} \text{Im} \rho_{ex} &= \frac{1}{2} \sin 2\theta_0 \sin \omega t (\rho_{ee}^0 - \rho_{xx}^0) \\ &+ \cos 2\theta_0 \sin \omega t \text{Re} \rho_{ex}^0 \\ &+ \left[1 - 2 \sin^2 \frac{\omega t}{2} \right] \text{Im} \rho_{ex}^0, \end{aligned} \quad (17)$$

where ρ_{ij}^0 denotes the initial density matrices of neutrinos (the i and j indexes take either e or x).

In this test, we adopt the following mass and mixing parameters: $\Delta m^2 = (-)2.45 \times 10^{-15} \text{ MeV}^2$ and $\sin^2 \theta_0 = 2.24 \times 10^{-2}$ (2.26×10^{-2}) for the normal mass ordering (the inverted mass ordering) (Olive & Particle Data Group 2014). Hereafter, we refer to each mass hierarchy as NO and IO, respectively. The neutrino energy (E_ν) is assumed to be 20 MeV. As an initial condition, we emit a single MC particle (the flight direction can be arbitrary chosen) with setting a purely ν_e state, i.e., the ee component of q is 1 and others are set to be zero⁷. During the evolution, time step (Δt) is constant with $\omega \Delta t / 2\pi = 10^{-3}$.

Figures 3 show the time evolution of each matrix element of q in cases with NO (left panel) and IO (right panel). The QKE-MC results are shown in solid lines while the analytical solutions are in black dashed lines. In the bottom figures, the errors from analytic solutions are displayed. As shown in these figures, QKE-MC results are good agreement with analytic solutions for both mass hierarchies.

Figure 4 portrays the convergence of our code with respect to Δt . In this check, we compare q_{ee} at the time of $\omega t / 2\pi = 10$ between the numerical (QKE-MC) and analytical solutions. We confirm that our code achieved a 4th-order convergence. We note that, the round-off-error is seen in the case with $\omega \Delta t / 2\pi = 10^{-4}$, which results in degrading the convergence.

The norm of polarization vector, $|P|$, is a conserved quantity in this test; hence, it is also useful to measure the accuracy of our code. In Fig. 5, we show the time evolution of $|1 - |P||$ (we note that $|P|$ is 1 at the initial condition) for two different time step ($\omega \Delta t / 2\pi = 10^{-2}$ and 10^{-3}). We display the results with NO oscillation in the figure. This result suggests that $|P|$ is well conserved in the test, and that the accuracy is improved with decreasing Δt .

6. NEUTRINO OSCILLATION IN MATTER

As long as the matter potential, H_{mat} , is static and homogeneous, we can obtain exact solutions of QKE (with respect to the time evolution of the system) with vacuum and matter potentials. If only electrons surround neutrinos, the exact solution can be obtained by replacing $\theta_0 \rightarrow \theta_m$ and $\omega \rightarrow \omega_m \equiv \Delta m_m^2 / 2E_\nu$ in Eqs. 14-17,

⁷ Since it is a linear system (see also Eq. 1 or 8), the result is scale free, indicating that an arbitrary positive value can be chosen.

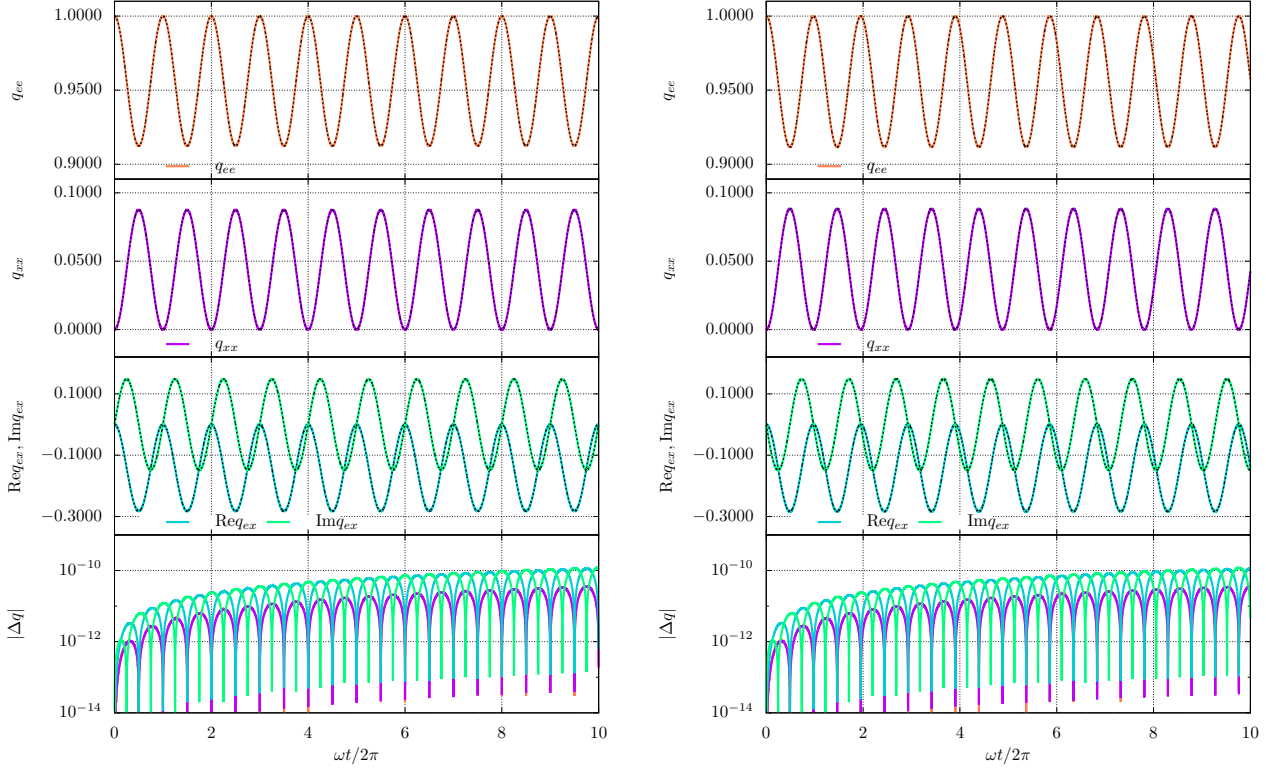


Figure 3. The time evolution of each matrix element of q_s in the test of vacuum oscillations. Left and right panels show the normal and inverted mass ordering, respectively. Solid lines represented numerical solutions and dashed black lines are analytical solutions. In the bottom panel, the errors from the analytical solutions are displayed.

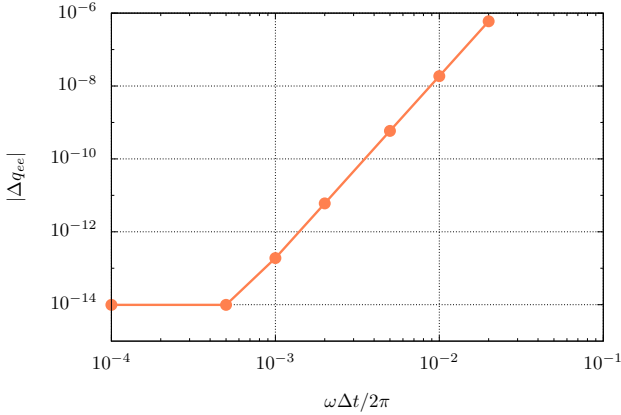


Figure 4. Numerical error as a function of Δt for tests of vacuum oscillation in the case of the normal mass ordering (NO).

where θ_m and Δm_m^2 can be written as,

$$\sin 2\theta_m = \frac{\sin 2\theta_0}{\sqrt{(\cos 2\theta_0 \pm A)^2 + \sin^2 2\theta_0}}, \quad (18)$$

$$\Delta m_m^2 = \Delta m^2 \sqrt{(\cos 2\theta_0 \pm A)^2 + \sin^2 2\theta_0}, \quad (19)$$

with $A = 2\sqrt{2}G_F n_e E_\nu / \Delta m^2$, where n_e denotes the number density of electrons. Regarding the sign in front

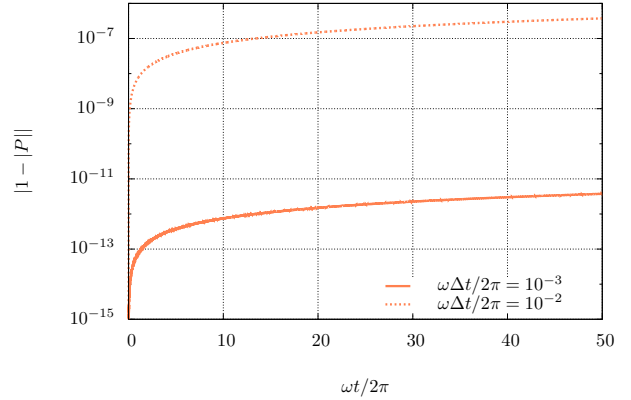


Figure 5. The time evolution of $|1 - |P||$ for the test of vacuum oscillation. We show the results for simulations with two different time resolutions: $\omega\Delta t/2\pi = 10^{-3}$ (solid line) and 10^{-2} (dashed line). In this figure, we assume NO for mass hierarchy.

of A in Eqs. 18 and 19, positive and negative signs are taken in the cases of neutrinos and anti-neutrinos, respectively. As shown in Eq. 18, the large mixing (resonance) occurs when the denominator of right hand side of Eq. 18 is zero. This is equivalent to the condition of

$n_e = (-)n_{e0}$ for (anti-)neutrinos, where

$$n_{e0} = \frac{\Delta m^2 \cos 2\theta_0}{2\sqrt{2}G_F E_\nu}. \quad (20)$$

In Fig. 6, we show the time evolution of q_{ee} for various cases of n_e . In these tests, the initial condition of neutrinos is the same as that used in the test of vacuum oscillation (see Sec. 5). The result of analytic solutions are plotted with black dashed lines. This figure suggests that our code accurately demonstrates the neutrino oscillation in matter.

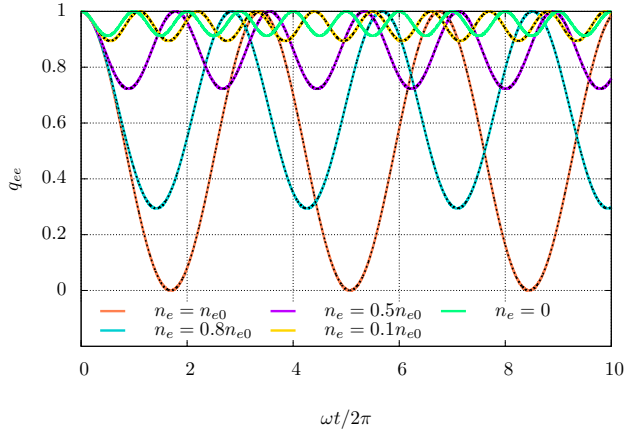


Figure 6. We show the time evolution of ν_e for the test of MSW neutrino oscillation. Color lines show the results for different n_e , and the black dashed lines represent the analytic solutions

. In this figure, we assume NO for mass hierarchy.

It may be interesting to see the resonance case ($n_e = n_{e0}$) in more detail. Figs. 7 display the same quantities as displayed in Figs. 3. Fig. 8 shows the result of convergence check. The error is measured at $t = 2\pi/\omega \times 10$, which is the same as that in the vacuum test (see also Fig. 4). These tests suggest that the MSW resonance can be handled accurately in our QKE-MC solver.

7. COLLECTIVE OSCILLATION

We perform three representative tests for collective neutrino oscillations. One of them is a collective neutrino oscillation in isotropic angular distributions. This is the same problem as done in Hannestad et al. (2006). The result is summarized in Sec. 7.1. In Sec. 7.2, we test a two-beam collective oscillation following Chakraborty et al. (2016). We compare the results with the linear analysis quantitatively. In Sec. 7.3, we carry out a test of fast flavor conversion. We evolve the system, in which the anisotropic neutrino distribution with a single ELN-crossing is set as an initial

condition, by using QKE-MC solver. It should be mentioned that, although the physical setup is exactly the same as one of the simulations in Shalgar & Tamborra (2021a), our results are inconsistent with them. To address the issue, another simulation is carried out for the same problem but using an independent code (finite-difference method). Our two simulations provide consistent results each other; indeed, we confirm that both simulations converge to the same results with increasing resolutions.

7.1. isotropic distribution

In this test, we assume that neutrinos and anti-neutrinos have the same isotropic distributions. Regarding the matter potential, we assume $\bar{n}_e = n_x = \bar{n}_x = 0$. Following the convention of Hannestad et al. (2006), we describe the QKE by using polarization vectors (see also Eq. 12),

$$\begin{aligned} \frac{\partial}{\partial t} \mathbf{P}' &= [\omega \mathbf{B} + \lambda \mathbf{L} + \mu (\mathbf{P}' - \bar{\mathbf{P}}')] \times \mathbf{P}', \\ \frac{\partial}{\partial t} \bar{\mathbf{P}}' &= [-\omega \mathbf{B} + \lambda \mathbf{L} + \mu (\mathbf{P}' - \bar{\mathbf{P}}')] \times \bar{\mathbf{P}}', \end{aligned} \quad (21)$$

with $\lambda = \sqrt{2}G_F n_e$, $\mu = \sqrt{2}G_F n_\nu$ ($n_\nu = n_{\nu_e} = n_{\bar{\nu}_e}$) and $\mathbf{L} = \text{diag}[1, 0]$. In the expression, we normalize the polarization vectors as $\mathbf{P}' = \mathbf{P}/n_\nu$ and $\bar{\mathbf{P}}' = \bar{\mathbf{P}}/n_\nu$.

As the first test, we ignore the matter potential, i.e., λ is set to be zero. In this case, Eq. 21 can be rewritten as,

$$\begin{aligned} \dot{\mathbf{Q}} &= \mu \mathbf{D} \times \mathbf{Q}, \\ \dot{\mathbf{D}} &= \omega \mathbf{B} \times \mathbf{Q}, \end{aligned} \quad (22)$$

with $\mathbf{Q} = \mathbf{P} + \bar{\mathbf{P}} - \omega \mathbf{B}/\mu$ and $\mathbf{D} = \mathbf{P} - \bar{\mathbf{P}}$. As shown in Hannestad et al. (2006), we have four conserved quantities in the system: $|\mathbf{Q}|$, $\mathbf{D} \cdot \mathbf{B}$, $\mathbf{D} \cdot \mathbf{Q}$, $H \equiv \omega \mathbf{B} \cdot \mathbf{Q} + \mu |\mathbf{D}|^2/2$. They are useful to check the accuracy of our QKE-MC solver. Setting the initial condition with $\mathbf{P}'(0) = \bar{\mathbf{P}}'(0) = (0, 0, 1)$, we obtain

$$\mathbf{D} = \frac{1}{\mu} \frac{\mathbf{Q} \times \dot{\mathbf{Q}}}{|\mathbf{Q}|^2}. \quad (23)$$

Eq. 23 is an analogous equation to that describing the dynamics of charged particles propagating in electric field. It can be further cast into the following form,

$$\ddot{\phi} = -\omega \mu Q \sin(\phi + 2\theta_0), \quad (24)$$

with $\mathbf{Q} = Q(\sin \phi, 0, \cos \phi)$. This suggests that the dynamics is analogous to a pendulum. We refer readers to Hannestad et al. (2006) for more detail.

In the numerical setup of QKE-MC solver, we inject one MC particle with $E_\nu = 20$ MeV initially with purely

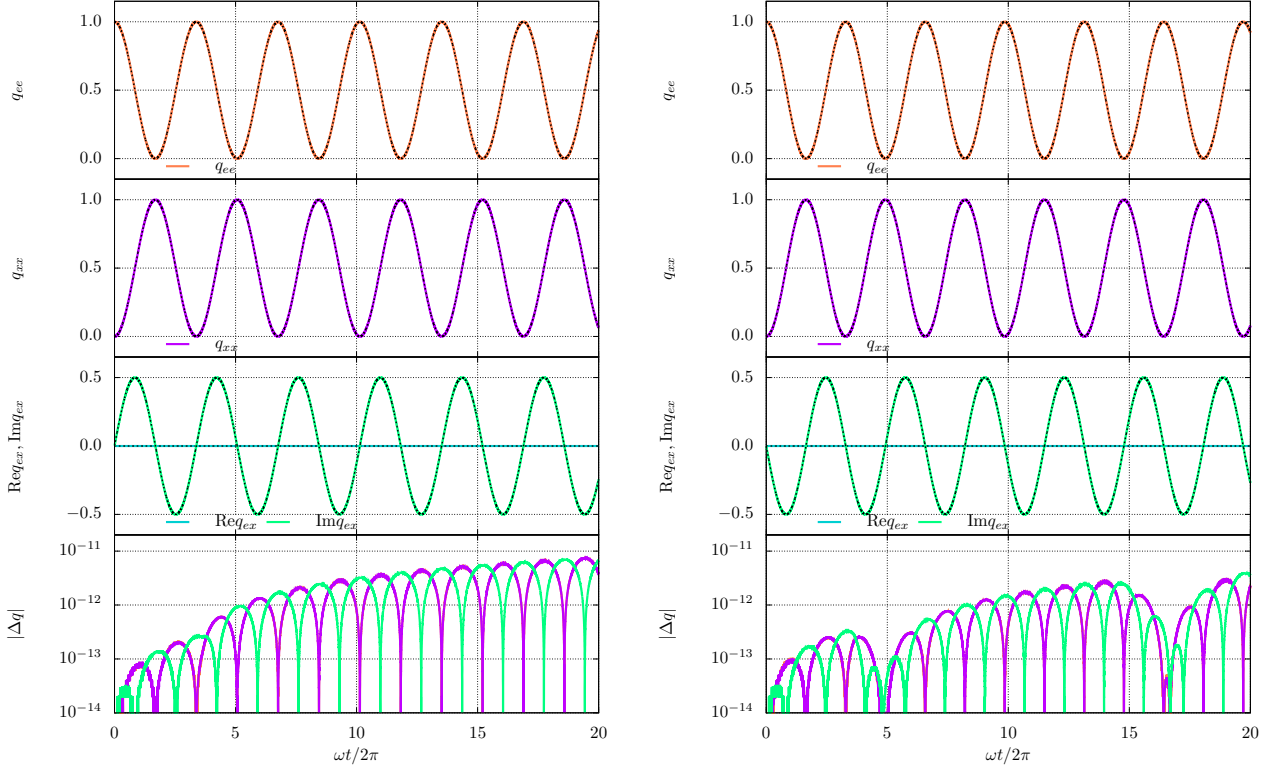


Figure 7. The same as Fig. 3 but for MSW effects. We adopt $n_e = n_{e0}$ (resonant oscillation). Left and right panels show the results with normal and inverted mass ordering, respectively.

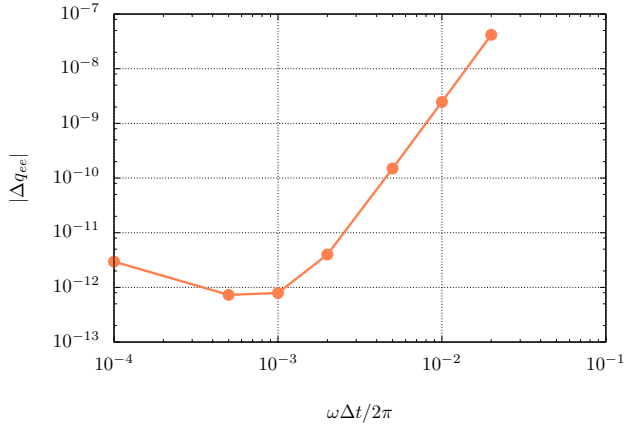


Figure 8. The same as Fig. 4 but for a MSW test. We adopt $n_e = n_{e0}$ (resonant oscillation) in these simulations.

ν_e and $\bar{\nu}_e$ states. We note that, their flight direction can be arbitrary chosen, meanwhile we ignore the angular dependence of neutrinos in the evaluation of the neutrino self-interaction potential during the time evolution. By virtue of the prescription, only the isotropic component of the potential remains. It should be noted that it is possible to set isotropic angular distributions of neutrinos by generating many MC particles, and compute the self-interaction potential without the above prescription. On the other hand, neutrino flight di-

rections of each MC particle are constant with time, and the neutrino oscillation is identical among all MC particles. This indicates that computations of many MC particles are wasteful. Our prescription does not compromise the analysis and saves the computational resource. The number of neutrinos, i.e., the ee component of q (and \bar{q}) is chosen so that μ becomes 10ω ($\Delta m^2 = -2.45 \times 10^{-15} \text{ MeV}^2$). The mixing angle is set as $\theta_0 = 0.01$ to reproduce the result of Hannestad et al. (2006). In this test, we adopt a constant time step with $\mu\Delta t = 10^{-3}$.

Figure 9 portrays the time evolution of the z -components for \mathbf{P} and $\bar{\mathbf{P}}$ computed by our QKE-MC solver. This is in good agreement with the result of Hannestad et al. (2006) (see Fig.1 in their paper). To see the capability of our code more quantitatively, we compare to the solutions obtained by solving Eq. 24; the results are summarized in Fig. 10. We confirm that our QKE-MC solver provides a consistent result with the solutions of Eq. 24; indeed, the deviation ($|\Delta Q_z|$) is $\lesssim 10^{-3}$ up to the time of $\omega t = 80$ (see the bottom panel of Fig. 10).

Figure 11 displays the time evolution of conserved quantities. In this figure, we add the result with $\mu\Delta t = 10^{-2}$ to see the dependence of time step. All the quantities, or $|\mathbf{P}|$, $|\mathbf{Q}|$, H , $\mathbf{D} \cdot \mathbf{B}$ and $\mathbf{D} \cdot \mathbf{Q}$, are well conserved

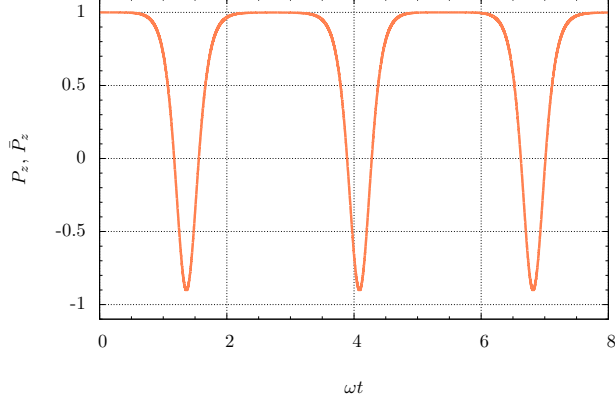


Figure 9. The time evolution of the z-components in polarization vectors in a test of isotropic collective neutrino oscillation without matter potential. We show the results for $\mu\Delta t = 10^{-3}$ in this figure. See also Fig.1 in Hannestad et al. (2006) that corresponds to a counterpart of this figure.

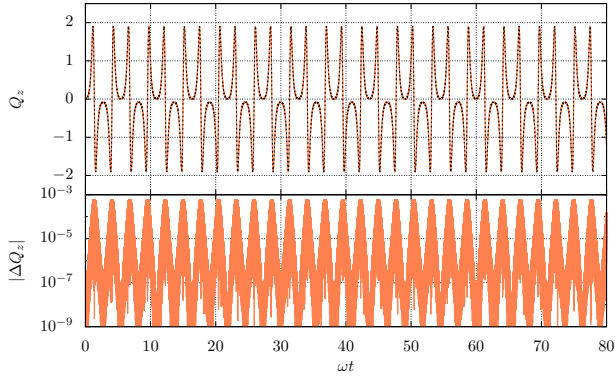


Figure 10. Time evolution of Q_z for a test of isotropic collective neutrino oscillation without matter potential. In the top panel, we compare the results between QKE-MC (orange-solid line) and those obtained by solving Eq. 24 (black-dashed line). The difference, $|\Delta Q_z|$, is displayed in the bottom panel. We adopt a constant time step ($\mu\Delta t = 10^{-3}$) in our QKE-MC simulation.

in our results, and we confirm that the smaller Δt tends to improve the accuracy of the conserved quantities.

As another test of isotropic collective neutrino oscillations, we include the matter term in addition to the self-interaction potential (see Eq. 21). Same as Hannestad et al. (2006), we vary the value of λ : $\lambda = 10^2\omega$, $10^3\omega$ and $10^4\omega$. Figure 12 shows the time evolution of P_z and \bar{P}_z obtained by our QKE-MC (see also Fig. 9 for comparison to the case without matter potential). We confirm that our results reproduce the same results reported in Hannestad et al. (2006) (see Fig.2 in the paper). This suggests that our code is capable of handling the collective neutrino oscillations in isotropic distributions.

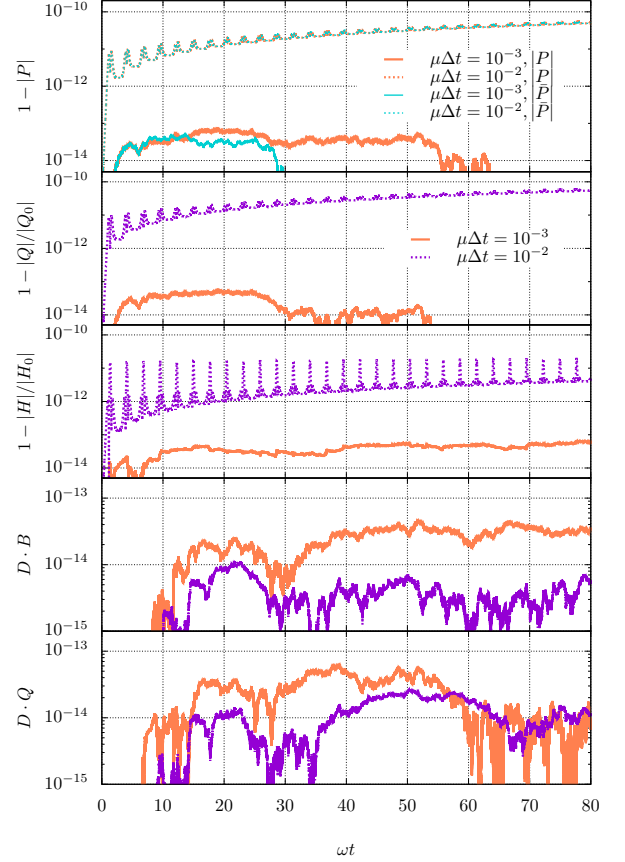


Figure 11. The time evolution of errors of conserved quantities for a test of isotropic collective neutrino oscillation without matter potential. From top to bottom, we display the results of $1 - |P|$, $1 - |Q|/|Q_0|$, $1 - H/H_0$, $D \cdot B$ and $D \cdot Q$, respectively. We show the results with two different time steps in our QKE-MC simulation: $\mu\Delta t = 10^{-3}$ (solid-line) and 10^{-2} (dashed-line).

7.2. Two-beam collective oscillation

We employ a two-beam model as a test of collective oscillation. In this model, neutrinos and anti-neutrinos, propagating in the opposite direction, intersect each other. The characteristics of flavor conversion has been well studied (see, e.g., Chakraborty et al. 2016). We also note that the dispersion relation of the instability can be written in a concise way (see below). Hence, we compare the result of QKE-MC simulation to the analytic solution in the linear regime.

Following Chakraborty et al. (2016), we give an overview of the derivation of eigen frequency. In the system, we obtain the time evolution of the number densities from QKE as,

$$i \frac{\partial n_{ex,1}}{\partial t} = \left(-\frac{\Delta m^2}{2E_\nu} - 2\sqrt{2}G_F \bar{n}_{ee,2} \right) n_{ex,1}$$

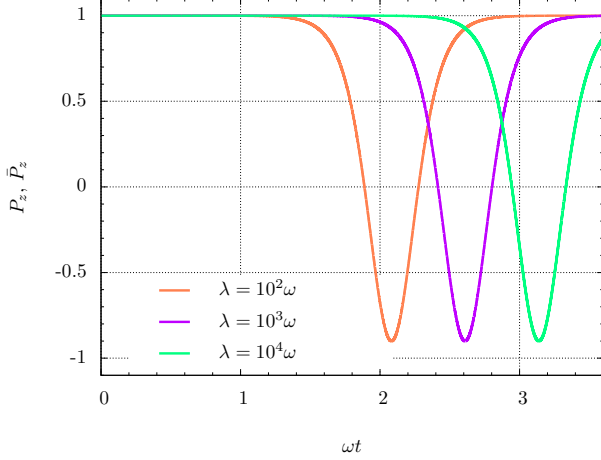


Figure 12. The same as Fig. 9 but for the test including matter potential. Different colors denote results for different values of matter potential: $\lambda = 10^2\omega, 10^3\omega$, and $10^4\omega$. We adopt a constant time step ($\mu\Delta t = 10^{-3}$) in this test.

$$+2\sqrt{2}G_F\bar{n}_{ex,2}^*n_{ee,1}, \quad (25)$$

$$i\frac{\partial\bar{n}_{ex,2}}{\partial t} = \left(-\frac{\Delta m^2}{2E_\nu} - 2\sqrt{2}G_F n_{ee,1}\right)\bar{n}_{ex,2} + 2\sqrt{2}G_F\bar{n}_{ex,1}^*\bar{n}_{ee,2}, \quad (26)$$

where indices 1 and 2 distinguishes the flight direction of neutrinos, i.e., specifying neutrinos and anti-neutrinos, respectively; we assume $\theta_0 = 0$ and a monochromatic neutrino energy with E_ν . It should be mentioned that we integrate over the momentum space in these equations. Before linearizing the equation, we define two new variables, g and S , as

$$n_i - \bar{n}_i^* = \frac{1}{2}\text{Tr}(n_i - \bar{n}_i^*) + \frac{g_i}{2} \begin{pmatrix} 1 & S_i \\ S_i^* & -1 \end{pmatrix}, \quad (27)$$

where $g_i = n_{ee,i} - n_{xx,i} - \bar{n}_{ee,i} + \bar{n}_{xx,i}$. In our test case, $g_1 = n_{ee,1}$, $g_2 = -\bar{n}_{ee,2}$, $n_{ex,1} = g_1 S_1/2$ and $\bar{n}_{ex,2} = -g_2 S_2^*/2$. By using the new variables, the linearized equations can be written as

$$i\frac{\partial S_1}{\partial t} = \left(-\frac{\Delta m^2}{2E_\nu} + 2\sqrt{2}G_F g_2\right)S_1 - 2\sqrt{2}G_F g_2 S_2, \quad (28)$$

$$i\frac{\partial S_2^*}{\partial t} = -\left(\frac{\Delta m^2}{2E_\nu} + 2\sqrt{2}G_F g_1\right)S_2^* + 2\sqrt{2}G_F g_1 S_1^*. \quad (29)$$

Adopting plane wave expansion with $S_i = Q_i \exp(-i\Omega t)$, the eigen frequency can be written as,

$$\Omega = \sqrt{2}G_F(g_1 + g_2) \pm \sqrt{2G_F^2(g_1 + g_2)^2 + \omega'(\omega' + 2\sqrt{2}G_F(g_1 - g_2))}, \quad (30)$$

with $\omega' = -\omega$. In this test, neutrino distributions are assumed to be homogeneous (see Chakraborty et al. 2016,

for more general cases). For convenience, we introduce an asymmetry parameter between neutrinos and anti-neutrinos, α . We rewrite the number densities of neutrinos and anti-neutrinos by using α as $n_{ee} = (1 + \alpha)n_t$ and $\bar{n}_{ee} = (1 - \alpha)n_t$, respectively, where n_t represents their average, i.e., $n_t = 0.5(n_{ee} + \bar{n}_{ee})$. The dispersion relation can be rewritten as,

$$\Omega_{\pm} = 2\alpha\mu' \pm \sqrt{(2\alpha\mu')^2 + \omega'(\omega' - 4\mu')}, \quad (31)$$

with $\mu' = \sqrt{2}G_F n_t$. The imaginary part of Ω has a non-zero value in cases with $(2\alpha\mu')^2 + \omega'(\omega' - 4\mu') < 0$. In this condition, the slow flavor instability kicks in. In other cases, the flavor conversion occurs periodically with constant frequencies. The corresponding eigenvector of Ω_- , for example, can be written as

$$\begin{pmatrix} Q_1 \\ Q_2 \end{pmatrix} = \begin{pmatrix} 2\mu'(\alpha - 1) \\ \omega' + 2\mu'(\alpha - 1) - \Omega_- \end{pmatrix} b. \quad (32)$$

This is used for an initial condition in our QKE-MC solver.

To reproduce the two-beam environment in our QKE-MC simulation, we prepare two MC particles. One of them is for neutrinos, and the other is for anti-neutrinos. The flight direction of each particle is opposite each other. The neutrino energy is set to be $E_\nu = 50$ MeV. To determine Δt , we compare the vacuum- and collective oscillation timescale at each time step, and then adopt the smaller one. We then multiply it by a factor of 10^{-4} . We demonstrate four simulations by changing α ($\alpha = 0$ and 0.5) and μ' ($\mu' = \omega'/8$ and $\omega'/2$). In this test, we adopt the value of mass difference: $\Delta m^2 = -2.45 \times 10^{-3} \text{eV}^2$. The corresponding time scale of $1/\omega$ is 2.69×10^{-5} s, and the number density of n_t with $\mu' = \omega'$ is $1.93 \times 10^{26} \text{cm}^{-3}$. The initial condition of q and \bar{q} is set so as to coincide with an eigenvector with Ω_- with $\text{Re}b = \text{Im}b = 10^{-6}/2\mu'(\alpha - 1)$ in Eq. 32.

Figure 13 shows the time evolution of the real part of n_{ex} in the linear regime ($|S| \ll 1$). Orange and black lines represent the QKE-MC results and those computed from the linearized QKE. Top and bottom panels show the results for $\mu' = \omega'/8$ and $\omega'/2$, where the former and latter systems are the stable and unstable with respect to slow flavor conversion. Regardless of the asymmetric parameter and stability, our QKE-MC code can accurately reproduce the analytic solutions in the linear phase.

7.3. fast flavor conversion in axisymmetric momentum space

As a test of fast flavor conversion, we carry out simulations with the same physical condition of Shalgar & Tamborra

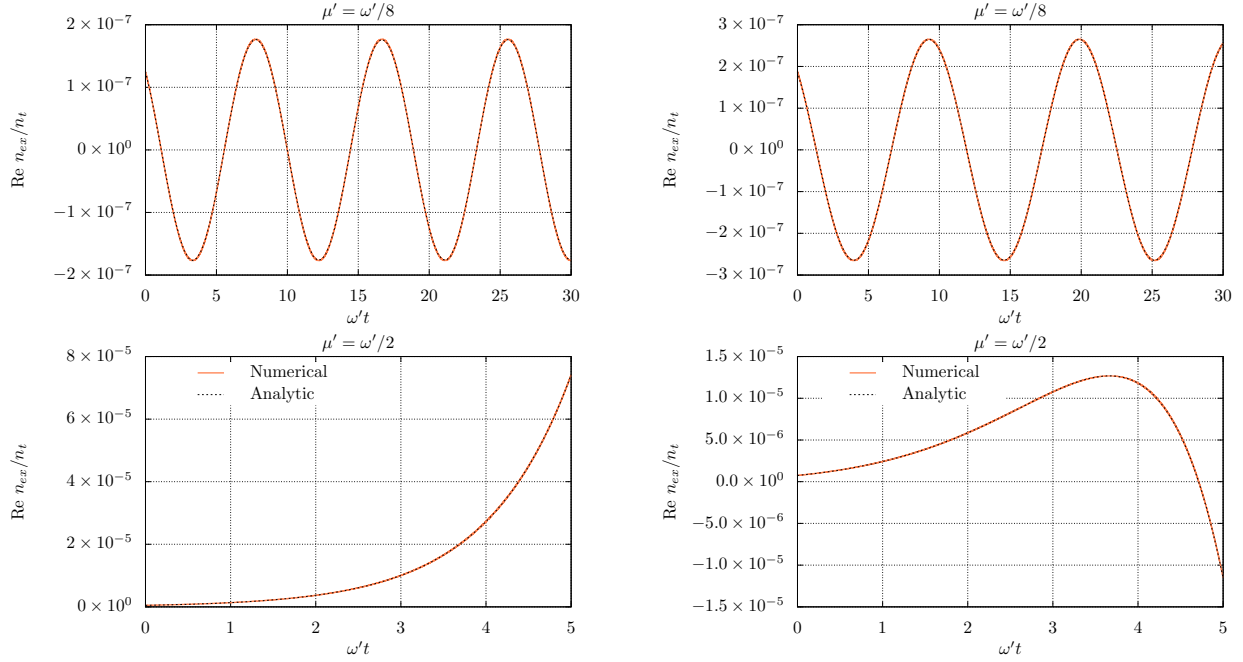


Figure 13. The time evolution of the real part of n_{ex} in the test of two-beam collective oscillation. In the left and right panels, we adopt the different asymmetric parameter, $\alpha = 0$ (left) and 0.5 (right). Orange and black lines denote the QKE-MC results and the those computed from eigen frequency, respectively. We show the results with two different μ' 's in top and bottom panels. The top and bottom panels correspond to the stable and unstable system to flavor conversion. See text for more detail.

(2021a), in which the angular distributions of ν_e and $\bar{\nu}_e$ has initially a single crossing in momentum space, indicating that it is unstable to fast flavor conversion. We apply our QKE-MC solver to evolve the system under homogeneous approximation, and then we compare the results to those in Shalgar & Tamborra (2021a). Despite of the same physical setup, we find that our results are inconsistent with theirs. We validate ours by comparing to results computed by another independent code.

In this test, we assume a monochromatic neutrino energy with E_ν and axial symmetry in momentum space. For convenience, we define the azimuthal-integrated density matrix as,

$$\rho_a(\theta_\nu) = \int \rho(\theta_\nu, \phi_\nu) d\phi_\nu. \quad (33)$$

The governing equation in the system can be written as

$$\begin{aligned} i \frac{\partial \rho_a}{\partial t} &= [H'_{\text{vac}} + H_{\text{mat}} + H'_{\nu\nu}, \rho_a], \\ i \frac{\partial \bar{\rho}_a}{\partial t} &= [H'_{\text{vac}} - H_{\text{mat}}^* - H'_{\nu\nu}, \bar{\rho}_a], \end{aligned} \quad (34)$$

with

$$\begin{aligned} H'_{\text{vac}} &= U \frac{1}{2E_\nu} \begin{pmatrix} m_1^2 & 0 \\ 0 & m_2^2 \end{pmatrix} U^\dagger, \\ H'_{\nu\nu} &= \sqrt{2} G_F \int \frac{d \cos \theta'_\nu}{(2\pi)^3} (1 - \cos \theta_\nu \cos \theta'_\nu) \end{aligned}$$

$$\times (\rho'_a - \bar{\rho}_a'^*). \quad (35)$$

We set an initial condition,

$$\begin{aligned} \rho_{ee,a0} &= 0.5 n_\nu, \\ \bar{\rho}_{ee,a0} &= \left[0.47 + 0.05 \exp \left(-(\cos \theta_\nu - 1)^2 \right) \right] n_\nu, \end{aligned} \quad (36)$$

where n_ν denotes the total number density of ν_e . We assume $\mu = 10^5 \text{ km}^{-1}$, $\theta_0 = 10^{-6}$, $\Delta m^2 = 2.50 \times 10^{-6} \text{ eV}^2$, and $E_\nu = 50 \text{ MeV}$, which leads to $\omega = 1.27 \times 10^{-4} \text{ km}^{-1}$. We note that this setup is the same as the case A in Shalgar & Tamborra (2021a).

For convenience, we provide the time scale under the choice of these parameters. They are $3.33 \times 10^{-11} \text{ s}$ and $2.67 \times 10^{-2} \text{ s}$ for neutrino self-interaction and vacuum oscillation, respectively. Since $\mu \gg \omega$ is satisfied, the neutrino oscillation is dominated by fast flavor conversion⁸.

In QKE-MC simulations, we inject MC particles isotropically. To see the convergence, we change the total number of MC particle as 64, 128, 256 and 512. Following Eq. 36, we determine the values of q and \bar{q} in each MC particle. During the time evolution, Δt is not

⁸ However, the vacuum term is important to generate a seed perturbation in the system. Since there are no neutrinos in the mixing flavor-states at initial time, the flavor conversion does not occur without the vacuum contribution.

constant. It is essentially determined by the maximum difference of ρ_a and $\bar{\rho}_a$ at each time step. We compute the effective ELN number density by assuming that the maximum difference is distributed isotropically. This gives a conservative time scale of the fast flavor conversion. We further divide it by a factor of dt_{fac} . We adopt $dt_{\text{fac}} = 50$ as a representative case. It should be mentioned that the MC particles do not change their momentum state in this test due to no collision terms, indicating that the statistical noise is not an issue in this problem. Hence, we do not need a special treatment to reduce the noise (see also Sec. 3.2).

Figure 14 shows the time evolution of a transition probability, which is defined by

$$\langle P_{ex} \rangle = 1 - \frac{\int \rho_{ee,a} d\cos\theta_\nu}{\int \rho_{ee,a0} d\cos\theta_\nu}. \quad (37)$$

Solid lines represent our results and color distinguishes the total number of MC particles. In the linear phase ($\lesssim 10^{-6}$ s), the resolution dependence (with respect to the total number of neutrinos) is minor; indeed the first peak profile in Fig. 14 is almost identical among all simulations. However, the deviation is obvious at the latter phase; the peak profile in the low resolution tends to appear earlier. On the other hand, we find no clear differences between the simulation of 256 and 512 MC particles up to the third peak.

In Shalgar & Tamborra (2021a), there is a counterpart figure, the blue line in the top left panel of Fig. 2 in their paper, to our Fig. 14. By comparing between the two results, the flavor conversion in their simulation tends to evolve slower than ours; for instance, the first peak of $\langle P_{ex} \rangle$ appears at $t \sim 0.6 \times 10^{-5}$ s. The discrepancy may suggest that our QKE-MC solver potentially generates artifacts due to its numerical treatments, requiring further exploration. We, hence, perform another simulation, in which we solve QKE with polarization vectors (see Eq. 12) by using finite-difference method. This is a deterministic- and mesh-based solver, indicating that the numerical artifacts inherent in our MC solver are not involved. We carry out two simulations with two different resolutions; the high resolution simulation adopts $\Delta t = 0.5\text{cm}/c$ and 256 angular grids, while the low resolution one adopts $\Delta t = 1\text{cm}/c$ and 128 angular grids. If the MC code has some issues, the detailed comparison between the two independent code is expected to reveal the origin of the discrepancy.

However, the finite difference method shows a consistent result with QKE-MC, which can be seen in Fig. 14 (black dashed- and dashed lines). It should also be mentioned that the difference between both codes becomes smaller with increasing resolutions. This detailed com-

parison lends confidence to our QKE-MC code. Our result calls into question the result of Shalgar & Tamborra (2021a), although addressing the issue is beyond the scope of this paper.

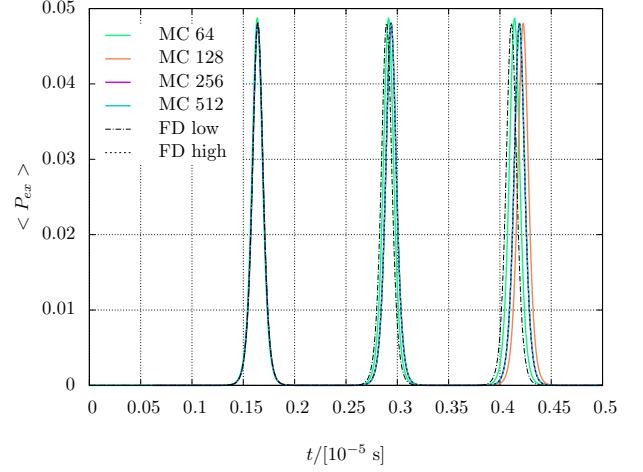


Figure 14. The time evolution of transition probability $\langle P_{ex} \rangle$ for a test of fast flavor conversion (Sec. 7.3). Solid lines represent QKE-MC results and the color distinguishes the total number of MC particles. Black lines denote results of finite-difference solver. The line type distinguishes the resolution. The high resolution case adopts 256 angular grids and $\Delta t = 0.5\text{cm}/c$, while the low resolution one uses 128 angular grids and $\Delta t = 1\text{cm}/c$. c denotes the speed of light in cgs unit.

To see the flavor conversion in more detail, we display the time evolution of neutrino angular distributions computed by our QKE-MC solver up to the time of the first peak in Fig. 15. In this figure, we show the result with 256 MC particles. As shown in the plot, the flavor conversion occurs around the ELN crossing point; the qualitative trend is the same as that found in Shalgar & Tamborra (2021a).

Finally, we check the dependence of Δt , that can be controlled by dt_{fac} . The results are displayed in Figure 16. We vary dt_{fac} from 1 to 50. We find that $dt_{\text{fac}} = 5$ provides the sufficient time resolution to this model. This also provides the consistent result with that obtained by the high resolution simulation of finite-difference method.

8. QKE WITH SCATTERING PROCESS

In this section, we apply our QKE-MC solver to problems including collision term. We pay special attention to scattering processes in this paper; there are mainly two reasons. One of them is that the scattering process is essentially the combined process of emission and absorption, indicating that this test provides

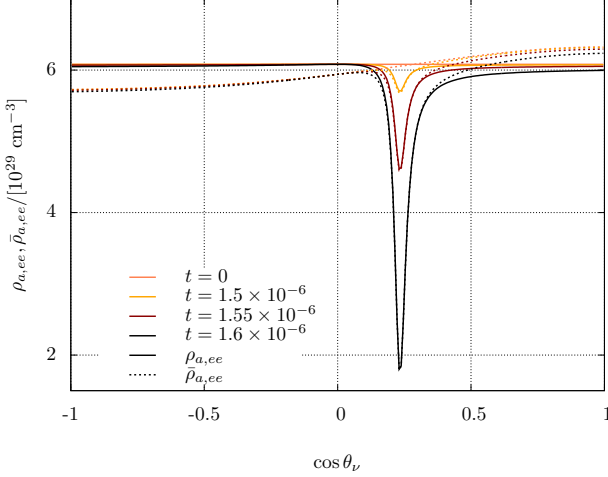


Figure 15. The time evolution of neutrino angular distributions for a test of fast flavor conversion (Sec. 7.3). We display the result up to the time of the first peak. Color distinguishes the time. Solid and dashed lines denote $\rho_{a,ee}$ and $\bar{\rho}_{a,ee}$, respectively. In this figure, we show the result of QKE-MC simulation with 256 MC particles.

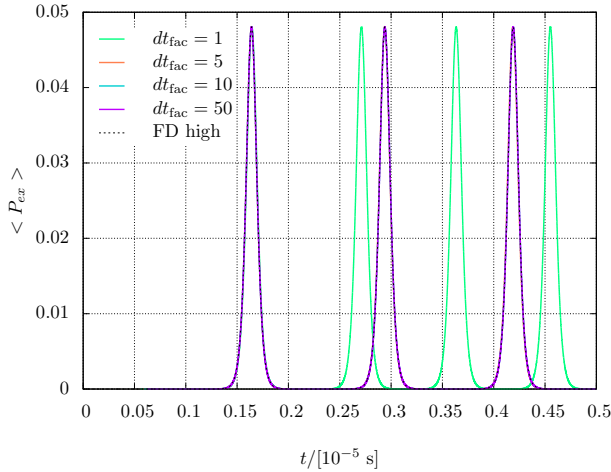


Figure 16. The Δt dependence of $\langle P_{ex} \rangle$ evolution. Different colors denote the results with different time resolution: $dt_{fac} = 1, 5, 10$ and 50 (see text for the definition of dt_{fac}). For comparison, the result of the high resolution simulation of finite-difference solver is also shown in black dashed line.

a good validation for these processes. The other reason is that roles of scattering in collective neutrino oscillations is gaining increased attention from the community (Shalgar & Tamborra 2021a; Martin et al. 2021; Johns 2021). Following the previous studies, we focus on an isoenergetic scattering in QKE. We note that the blocking factor in isoenergetic scatterings is exactly canceled

between in- and out-scatterings⁹. Although we postpone more detailed investigations on QKE with collision terms, this study has a role of the pilot study for them.

8.1. Test for scattering module

Before presenting a code test for a coupling system between neutrino oscillations and scatterings, we carry out another test to see the capability of scattering module implemented in our QKE-MC solver. As we described in Sec. 3.2, we change numerical treatments of scattering from our classical MC solver, indicating that the capability needs to be tested. We perform a cross-validation study by using our classical MC solver.

The detail of this test is as follows. We set anisotropic neutrino distributions on the monochromatic neutrino energy as an initial condition. The angular distribution of neutrinos is the same as that used for $\bar{\nu}_e$ in another test of fast flavor conversion (see Eq. 36 in Section 7.3). We follow the evolution of the system by using two codes: QKE-MC solver and classical MC solver. We consider the homogeneous system and incorporate isoenergetic scattering (see below for the reaction rate). We note that the oscillation module is turned off in the simulation by the QKE-MC solver.

In QKE-MC solver, we adopt 2,000 MC particles. In each particle, ee component of q is finite but others are zero. The reaction rate is $C = 0.05 \text{ km}^{-1}$. In this simulation, we apply EMFP method to reduce the statistical noise. We vary the parameter a as 10^{-2} , 10^{-3} and 10^{-4} . We note that simulations with the smaller value of a reduce more noise but become more computationally expensive (since the frequency of scattering for each MC particle increases with decreasing a , see Sec. 3.2 for the detail). On the other hand, the memory capacity is not pressed, that enables us to run the simulation on standard workstations. To reduce the computational cost, the newly generated MC particles due to scatterings on each time step are combined promptly to the adjacent ones. Although this prescription smears out the small angular structure of neutrinos, such a detailed structure is out of the scope of this test. In the classical MC transport (Kato et al. 2020), on the other hand, we use 10^5 MC particles and run 200 simulations with the identical initial condition. The resultant statistics is high enough

⁹ The blocking factor needs to be evaluated appropriately when we apply our code to emission-, absorption- and non-isoenergetic scattering processes. To do this, the energy volume in momentum space needs to be taken into account (to compute the density matrix), indicating that the monochromatic approximation can not be applied in the system. In fact, the delta function in the energy spectrum of neutrinos (corresponding to the monochromatic approximation) violates the characteristics of Fermions.

to quantitatively capture the time evolution of angular distributions of neutrinos.

Figure 17 shows the time evolution of the neutrino angular distribution, illustrating that scatterings isotropize the angular distribution of neutrinos. We find that the statistics is improved with reducing a . The result with $a = 10^{-4}$ is almost identical to that obtained from classical MC solver. This is a strong evidence that the EMFP method works well without degrading physical fidelity.

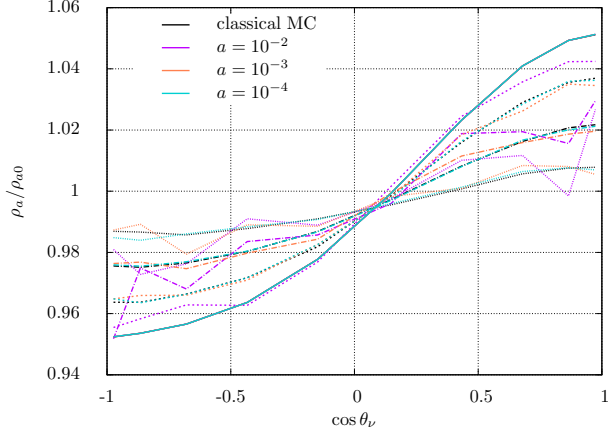


Figure 17. The time evolution of neutrino angular distributions in a test of scattering module (Sec. 8.1). Color distinguishes the model: purple ($a = 10^{-2}$ with QKE-MC), orange ($a = 10^{-3}$ with QKE-MC), light blue ($a = 10^{-4}$ with QKE-MC), and black (classical MC). Line-type distinguishes the time snapshot: $t/t_m = 0, 0.3, 0.75, 1.5$, where t_m denotes the mean free time ($t_m = 6.67 \times 10^{-5}$ s).

8.2. Fast flavor conversions with scatterings

As a final test, we demonstrate simulations for fast flavor conversion with scatterings. The physical setup is similar to that in Shalgar & Tamborra (2021a). As shown in Sec. 7.3, however, our results are inconsistent with them in cases without scatterings, indicating that a detailed comparison to their results is not meaningful. We, hence, take another way to validate our results. In this test, we focus on the early phase (the flavor conversion growth exponentially), and provide clear physical interpretations to the dynamics. For a quantitative assessment, we compare the growth rate of flavor conversion in our QKE-MC simulation to an empirical (analytic) formula given by Morinaga et al. (2020).

We start with describing the governing equation of the system. Following the convention used in Sec. 7.3, we rewrite the QKE as,

$$i \frac{\partial \rho_a}{\partial t} = [H'_{\text{vac}} + H_{\text{mat}} + H'_{\nu\nu}, \rho_a]$$

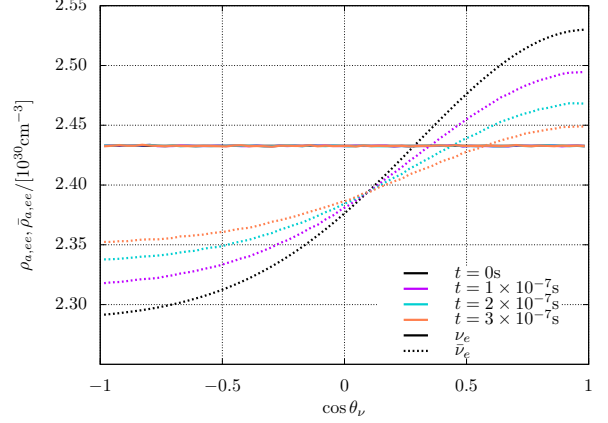


Figure 18. The time evolution of the angular distributions for ν_e (solid) and $\bar{\nu}_e$ (dashed) for a test of fast flavor conversion with scatterings. Different colors denote different time steps.

$$+ \int_{-1}^1 C \rho_a d \cos \theta'_\nu - \int_{-1}^1 C \bar{\rho}_a d \cos \theta'_\nu, \quad (38)$$

$$i \frac{\partial \bar{\rho}_a}{\partial t} = [H'_{\text{vac}} - H_{\text{mat}}^* - H_{\nu\nu}^*, \bar{\rho}_a] + \int_{-1}^1 C \bar{\rho}_a d \cos \theta'_\nu - \int_{-1}^1 C \rho_a d \cos \theta'_\nu, \quad (39)$$

where C represents a scattering rate. In this test, we assume that C is constant (no angular dependence), and we adopt $C = 10 \text{ km}^{-1}$ ¹⁰. It should be mentioned that a large number of MC particles is necessary compared to the case without scatterings (see Sec. 7.3). This is due to the fact that the statistical noise makes the simulation troublesome in this test. Following the prescriptions presented in Sec. 3.2, we reduce the noise by a smoothing method (in computations of self-interaction potential) and EMFP method. As a reference, we adopt the number of MC particles, the number of angular grids (N_θ) for the smoothing, and EMFP parameter (a) are 32,000, 64, and 10^{-5} , respectively. We show that this provides a sufficient resolution up to the time of end of our simulation (3×10^{-7} s). The resolution dependence is also discussed in this section.

¹⁰ In order to clearly see the impact of scattering in flavor conversion, the rate is relatively high (10 times higher than the model of the highest rate in Shalgar & Tamborra (2021a)). It should be mentioned, however, that we do not make a detailed comparison to their results; hence, the increase of the rate does not compromise our analysis.

Figure 18 shows the time evolution of the angular distributions for ν_e and $\bar{\nu}_e$. The former has an isotropic distribution initially, whereas the latter has an anisotropic distribution (see black lines). This figure illustrates that $\bar{\nu}_e$ angular distribution is isotropized with time, and the ELN crossing point changes with time (approaching to $\cos\theta_\nu = 1$). On the other hand, ν_e distribution does not evolve, indicating that the flavor conversion is subtle. This suggests that the remarkable change of angular distributions of $\bar{\nu}_e$ is due to scatterings.

To see the impact of scatterings on fast flavor conversion, we show the time evolution of off-diagonal component of ρ_a and $\bar{\rho}_a$ in Fig. 19. We pick up three different angular positions in the figure. This figure illustrates that both the oscillation amplitude and the growth rate in flavor conversion are suppressed by scatterings regardless of neutrino and anti-neutrinos. This may be attributed to the fact that the ELN angular distribution evolves to an isotropic distribution by scatterings (see Fig. 18), i.e., the amplitude of ELN crossing decreases with time. As discussed in Richers et al. (2021), the reduction of the amplitude of ELN crossing may account for the suppression. We reckon that there is another reason. As shown in Fig. 15, the fast flavor conversion occurs vigorously around the angular point of ELN crossing. On the other hand, the crossing point is migrated by scatterings (see Fig. 18), that works to disperse the growth of flavor conversions into wide angles. This would result in suppressing flavor conversion, unless the flavor conversion grows substantially during the stagnation of the crossing. This suggests an interesting possibility that the effect of scatterings hinges on the cross section of scatterings; more detailed investigation of the dependence is postponed to a future paper, though.

To strengthen the above argument, we compare the growth rate of fast flavor conversion obtained from the simulation to an empirical estimation proposed in our previous paper (Morinaga et al. 2020). We estimate the growth rate from our simulation as follows. We take the peak amplitude of off-diagonal component of ρ_a and $\bar{\rho}_a$ on each propagation direction (see, e.g., Fig. 19). We compute the slope (growth rate) by computing the difference at adjacent peak points and divided by the difference of time, and then take the angular average; the result is plotted in black line of Fig. 20. It should be noted that the growth rate is normalized by the one without scattering. Our result suggests that scatterings under the choice of the parameters reduce the growth of flavor conversion by $\sim 70\%$ at $t \sim 3 \times 10^{-7}$ s. The orange line in the same figure, on the other hand, portrays the

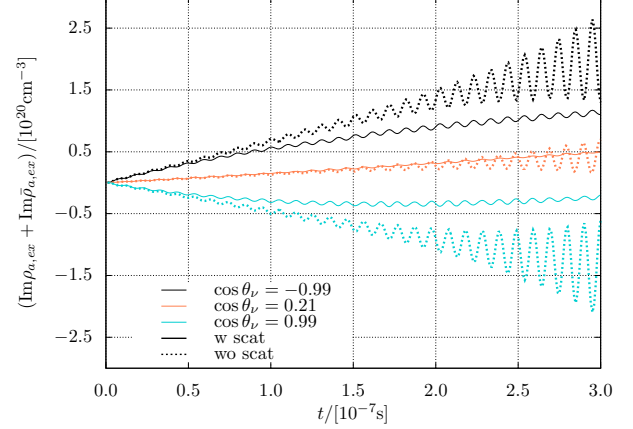


Figure 19. The time evolution of $\text{Im}\rho_{a,ex} + \text{Im}\bar{\rho}_{a,ex}$ at three different directions: $\cos\theta_\nu = -0.99$ (black), 0.21 (orange), and 0.99 (light blue), for a test of fast flavor conversion with scatterings. Color distinguishes angular directions. Solid and dashed lines represent the results with and without scatterings, respectively.

growth rate obtained by an empirical formula,

$$G \sim \sqrt{\left(\int_{\Delta\rho_a > 0} \Delta\rho_a d\cos\theta_\nu\right) \left(\int_{\Delta\rho_a < 0} \Delta\rho_a d\cos\theta_\nu\right)}, \quad (40)$$

with $\Delta\rho_a \equiv \rho_{a,ee} - \bar{\rho}_{a,ee}$ (see Morinaga et al. (2020)). We estimate the growth rate at each timestep by using $\Delta\rho_a$ obtained from the simulation. Although the two lines in Fig. 20 are slightly different from each other, the qualitative trend is essentially the same¹¹. This result suggests that the growth of flavor conversion is determined mainly by the angular distribution of ν_e and $\bar{\nu}_e$ at each instantaneous time, and that the isotropized ELN angular distribution due to scatterings is the major factor of the suppression (see Fig. 18). It should also be stressed that the reasonable agreement between the two results suggests that our QKE-MC solver works well to this problem.

Finally, we perform resolution studies. In the top panel of Fig. 21, we show the resolution dependence of N_θ . The reference value is 64, but we check the case with 128. It should be mentioned that the number of MC particles is also increased twice from the reference in the case with $N_\theta = 128$. This figure suggests that the difference between the two results is subtle. We also show the result without scatterings in the same figure, and the difference to the cases with scatterings is remarkable. Hence, the resolution of $N_\theta = 64$ is sufficient

¹¹ The deviation is mainly due to the accuracy of the empirical relation; indeed, the exact growth rate is quantitatively different from it. See Morinaga et al. (2020) for more detail.

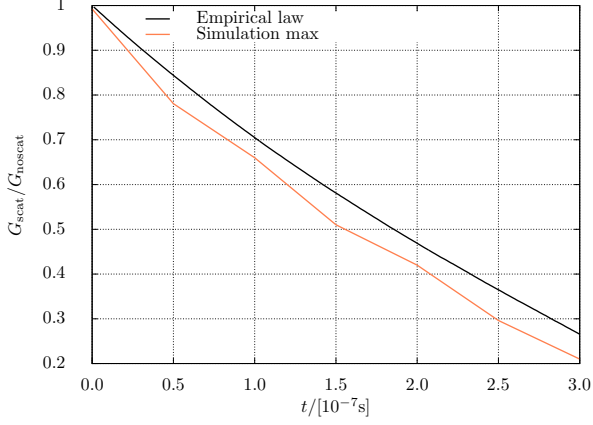


Figure 20. The time evolution of the growth rate ratio of fast flavor conversion between with and without scatterings. The ratio of < 1 indicates that the scattering suppresses fast flavor conversion. Orange line denotes the result computed by the time evolution of $\text{Im}\rho_{ex} + \text{Im}\bar{\rho}_{ex}$ from our QKE-MC simulation. The ratio computed from the empirical laws by Morinaga et al. (2020) is shown in black line. See text for more detail.

to capture the impact of scatterings qualitatively. In the middle panel of Fig. 21, we study the influence of statistical noise. For convenience, we use another variable, N , that is defined as the total number of MC particles divided by N_θ , i.e., it represents the total number of MC particles on each angular mesh. We find that $N = 500$ (reference value) is almost identical to the case with $N = 1000$, indicating that the statistical noise in our reference model does not compromise our results. It should be mentioned that the statistical noise is also reduced by the EMFP method. To see the impact more quantitatively, we run two additional simulations with $a = 10^{-4}$ and 10^{-6} , and the results are displayed in the bottom panel of Fig. 21. This figure suggests that the simulation with $a = 10^{-5}$ (reference value) is capable of providing a physically accurate result. This convergence test strengthens the reliability and capability of our new modules.

9. SUMMARY AND DISCUSSIONS

Recent years have witnessed a number of theoretical indications that collective neutrino oscillations commonly occur in CCSN and BNSM environments. This suggests that quantum kinetic features as neutrino oscillations needs to be taken into account, that potentially impact the global dynamics, nucleosynthesis, and neutrino signals. The full QKE neutrino transport is capable of describing both the microscopic and macroscopic dynamics. Numerical simulations may be the most general ab-initio approach. Although a considerable amount of efforts has been devoted to numerical

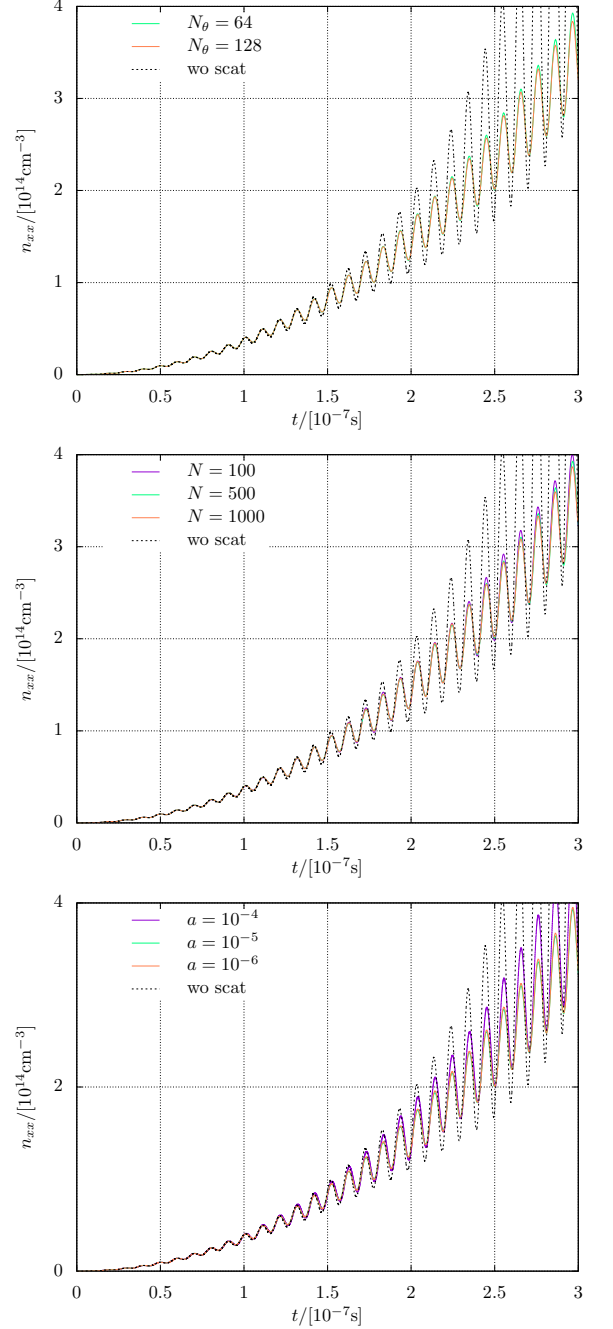


Figure 21. Resolution studies for the test of fast flavor conversion with scatterings (Sec. 8.2). Top: the number of angular grids (N_θ). Middle: the number of sample particles in each grid (N). Bottom: EMFP parameter (a). Color distinguishes different parameters for each resolution test. Green line corresponds to a reference calculation ($N_\theta = 64$, $N = 500$, $a = 10^{-5}$). For comparison, the results without scatterings are also plotted with black dashed lines.

simulations, the physically consistent treatments of flavor conversion, transport, and matter collision are technically difficult. In this paper, we propose a Monte Carlo (MC) method, which is potentially capable of handling all elements self-consistently. To this end, we updated our classical MC neutrino transport solver (Kato et al. 2020) to that of QKE. It is a representative probabilistic and particle method, indicating that our numerical models will be complementary to those simulated by other deterministic and mesh-based approaches.

In this QKE-MC solver, we handle neutrino flavor conversions by embedding a flavor degree of freedom into each MC particle (see Sec. 3.1). With the upgrades, numerical treatments of collision terms, in particular for scattering processes, need to be changed (see Sec. 3.2). New techniques are also developed to reduce statistical noise inherent in MC method. In this paper, we present a suite of code tests (see Secs. 5 to 8) to see the capability of each upgraded module by taking a cross-validation strategy, in which we reproduce the results reported in the previous literature. We show that our results are in good agreement with them for the tests of vacuum, matter, and collective oscillations. On the other hand, we found that our results are inconsistent with a previous study Shalgar & Tamborra (2021a) in tests of fast flavor conversions with/without isoenergetic scatterings. We validated our results by two approaches; (1) we applied another code (finite-difference scheme) to the same problem, and made a quantitative comparison; (2) we

employed some analytic (empirical) formula to compare our results of QKE-MC simulation. These complementary study have provided consistent results with ours, lending confidence to our QKE-MC solver.

It should be mentioned that the present paper is the first report describing the essential philosophy, design, and implementation of QKE neutrino transport by a MC approach. The detailed investigations of non-linear dynamics entangling neutrino oscillation, transport, and collision term are not the focus of this work but the greatest motivation. One of our short-term targets is to reveal the effects of collision terms, in particular for scatterings, on fast flavor conversions. We note that the results of numerical simulations by different groups are still at odds each other (see, e.g., Capozzi et al. 2019; Shalgar & Tamborra 2021a; Martin et al. 2021). Since our numerical method is fundamentally different from theirs, the results will provide an unique insight into the source of controversy. We have already started the long-term simulations of such a system, and the results will be reported in a forthcoming paper.

We are grateful to Sherwood Richers for valuable comments and discussions. C.K. is supported by Grant-in-Aid for Early-Career Scientists (No.20K14457) and Grant-in-Aid for Scientific Research on Innovative Areas (No.20H05240). T.M. is supported by JSPS Grant-in-Aid for JSPS Fellows (No. 19J21244) from the Ministry of Education, Culture, Sports, Science and Technology (MEXT), Japan.

REFERENCES

- Aartsen, M. G., Ackermann, M., Adams, J., et al. 2018, *Phys. Rev. Lett.*, 120, 071801
- Abbar, S. 2020, *JCAP*, 2020, 027
- Abbar, S. 2021, *Phys. Rev. D*, 103, 045014
- Abbar, S., Capozzi, F., Glas, R., Janka, H.-T., & Tamborra, I. 2021, *Phys. Rev. D*, 103, 063033
- Abbar, S., Duan, H., Sumiyoshi, K., Takiwaki, T., & Volpe, M. C. 2020, *Phys. Rev. D*, 101, 043016
- Abbar, S., & Volpe, M. C. 2019, *Physics Letters B*, 790, 545
- Abbott, B. P., Abbott, R., Abbott, T. D., et al. 2017, *ApJL*, 848, L12
- Abe, K., et al. 2014, *Nuclear Instruments and Methods in Physics Research A*, 737, 253
- Abe, K., Bronner, C., Haga, Y., et al. 2018a, *Phys. Rev. D*, 97, 072001
- Abe, K., Akutsu, R., Ali, A., et al. 2018b, *Phys. Rev. Lett.*, 121, 171802
- Acero, M. A., Adamson, P., Aliaga, L., et al. 2019, *PhRvL*, 123, 151803
- Adamson, P., Anghel, I., Aurisano, A., et al. 2014, *Phys. Rev. Lett.*, 112, 191801
- Aker, M., Altenmüller, K., Arenz, M., et al. 2019, *PhRvL*, 123, 221802
- Blaschke, D. N., & Cirigliano, V. 2016, *PhRvD*, 94, 033009
- Burrows, A., & Vartanyan, D. 2021, *Nature*, 589, 29
- Capozzi, F., Chakraborty, M., Chakraborty, S., & Sen, M. 2020, *Phys. Rev. Lett.*, 125, 251801
- Capozzi, F., Dasgupta, B., Mirizzi, A., Sen, M., & Sigl, G. 2019, *PhRvL*, 122, 091101
- Chakraborty, S., Choubey, S., Goswami, S., & Kar, K. 2010, *JCAP*, 2010, 007
- Chakraborty, S., Hansen, R. S., Izaguirre, I., & Raffelt, G. G. 2016, *JCAP*, 2016, 042
- Cherry, J. F., Carlson, J., Friedland, A., Fuller, G. M., & Vlasenko, A. 2012, *PhRvL*, 108, 261104
- Cherry, J. F., Carlson, J., Friedland, A., Fuller, G. M., & Vlasenko, A. 2013, *Phys. Rev. D*, 87, 085037

- Cherry, J. F., Fuller, G. M., Horiuchi, S., et al. 2020, *Phys. Rev. D*, 102, 023022
- Dasgupta, B., & Dighe, A. 2008, *PhRvD*, 77, 113002
- Dasgupta, B., Dighe, A., Raffelt, G. G., & Smirnov, A. Y. 2009, *PhRvL*, 103, 051105
- Dasgupta, B., Mirizzi, A., & Sen, M. 2017, *JCAP*, 2017, 019
- Dasgupta, B., Mirizzi, A., & Sen, M. 2018, *Phys. Rev. D*, 98, 103001
- Delfan Azari, M., Yamada, S., Morinaga, T., et al. 2019, *PhRvD*, 99, 103011
- . 2020, *PhRvD*, 101, 023018
- Dighe, A. S., & Smirnov, A. Y. 2000, *PhRvD*, 62, 033007
- Duan, H., Fuller, G. M., Carlson, J., & Qian, Y.-Z. 2006a, *PhRvD*, 74, 105014
- . 2006b, *PhRvD*, 74, 105014
- Esteban, I., Gonzalez-Garcia, M. C., Maltoni, M., Schwetz, T., & Zhou, A. 2020, *Journal of High Energy Physics*, 2020, 178
- Farag, E., Timmes, F. X., Taylor, M., Patton, K. M., & Farmer, R. 2020, *ApJ*, 893, 133
- Foglizzo, T., Kazeroni, R., Guilet, J., et al. 2015, *PASA*, 32, e009
- Fuller, G. M., Mayle, R. W., Wilson, J. R., & Schramm, D. N. 1987, *ApJ*, 322, 795
- Gallo Rosso, A., Vissani, F., & Volpe, M. C. 2018, *JCAP*, 2018, 040
- George, M., Wu, M.-R., Tamborra, I., Ardevol-Pulpillo, R., & Janka, H.-T. 2020, *Phys. Rev. D*, 102, 103015
- Glas, R., Janka, H.-T., Capozzi, F., et al. 2020, *Phys. Rev. D*, 101, 063001
- Hannestad, S., Raffelt, G. G., Sigl, G., & Wong, Y. Y. Y. 2006, *PhRvD*, 74, 105010
- Harris, J. A., Hix, W. R., Chertkow, M. A., et al. 2017, *ApJ*, 843, 2
- Horiuchi, S., & Kneller, J. P. 2018, *Journal of Physics G Nuclear Physics*, 45, 043002
- Janka, H.-T. 2012, *Annual Review of Nuclear and Particle Science*, 62, 407
- Johns, L. 2021, arXiv e-prints, arXiv:2104.11369
- Johns, L., Nagakura, H., Fuller, G. M., & Burrows, A. 2020, *PhRvD*, 101, 043009
- Kato, C., Nagakura, H., Hori, Y., & Yamada, S. 2020, *ApJ*, 897, 43
- Kawaguchi, K., Fujibayashi, S., Shibata, M., Tanaka, M., & Wanajo, S. 2021, *ApJ*, 913, 100
- Kotake, K., Takiwaki, T., Suwa, Y., et al. 2012, *Advances in Astronomy*, 2012, 428757
- Li, S. W., Roberts, L. F., & Beacom, J. F. 2021, *PhRvD*, 103, 023016
- Martin, J. D., Carlson, J., Cirigliano, V., & Duan, H. 2021, *PhRvD*, 103, 063001
- Martin, J. D., Carlson, J., & Duan, H. 2020a, *PhRvD*, 101, 023007
- Martin, J. D., Yi, C., & Duan, H. 2020b, *Physics Letters B*, 800, 135088
- Martínez-Pinedo, G., Fischer, T., & Huther, L. 2014, *Journal of Physics G Nuclear Physics*, 41, 044008
- Miller, J. M., Ryan, B. R., Dolence, J. C., et al. 2019, *PhRvD*, 100, 023008
- Mirizzi, A., Tamborra, I., Janka, H. T., et al. 2016, *Nuovo Cimento Rivista Serie*, 39, 1
- Mori, M., Suwa, Y., Nakazato, K., et al. 2021, *Progress of Theoretical and Experimental Physics*, 2021, 023E01
- Morinaga, T. 2021, arXiv e-prints, arXiv:2103.15267
- Morinaga, T., Nagakura, H., Kato, C., & Yamada, S. 2020, *Physical Review Research*, 2, 012046
- Müller, B. 2019, *Annual Review of Nuclear and Particle Science*, 69, 253
- . 2020, *Living Reviews in Computational Astrophysics*, 6, 3
- Nagakura, H. 2021, *MNRAS*, 500, 319
- Nagakura, H., Burrows, A., Vartanyan, D., & Radice, D. 2021, *MNRAS*, 500, 696
- Nagakura, H., Morinaga, T., Kato, C., & Yamada, S. 2019, *ApJ*, 886, 139
- O'Connor, E., Bollig, R., Burrows, A., et al. 2018, *Journal of Physics G Nuclear Physics*, 45, 104001
- Odrzywolek, A., & Heger, A. 2010, *Acta Phys. Polon. B*, 41, 1611
- Olive, K. A., & Particle Data Group. 2014, *Chinese Physics C*, 38, 090001
- Radice, D., Perego, A., Hotokezaka, K., et al. 2018, *ApJ*, 869, 130
- Richers, S., Nagakura, H., Ott, C. D., et al. 2017, *ApJ*, 847, 133
- Richers, S., Willcox, D. E., Ford, N. M., & Myers, A. 2021, *Phys. Rev. D*, 103, 083013
- Richers, S. A., McLaughlin, G. C., Kneller, J. P., & Vlasenko, A. 2019, *PhRvD*, 99, 123014
- Samuel, S. 1993, *Phys. Rev. D*, 48, 1462
- Sasaki, H., Kajino, T., Takiwaki, T., et al. 2017, *PhRvD*, 96, 043013
- Sawyer, R. F. 2005, *Phys. Rev. D*, 72, 045003
- Sekiguchi, Y., Kiuchi, K., Kyutoku, K., & Shibata, M. 2015, *PhRvD*, 91, 064059
- Shalgar, S., & Tamborra, I. 2021a, *PhRvD*, 103, 063002
- . 2021b, arXiv e-prints, arXiv:2106.15622
- Shibata, M., Nagakura, H., Sekiguchi, Y., & Yamada, S. 2014, *Phys. Rev. D*, 89, 084073

- Siegel, D. M., & Metzger, B. D. 2017, *PhRvL*, 119, 231102
- Sieverding, A., Müller, B., & Qian, Y. Z. 2020, *ApJ*, 904, 163
- Sigl, G. 1995, *Phys. Rev. D*, 51, 4035
- Sigl, G., & Raffelt, G. 1993, *Nuclear Physics B*, 406, 423
- Stapleford, C. J., Fröhlich, C., & Kneller, J. P. 2020, *PhRvD*, 102, 081301
- Suwa, Y., Sumiyoshi, K., Nakazato, K., et al. 2019, *ApJ*, 881, 139
- T2K Collaboration, & Abe, K. 2014, arXiv e-prints, arXiv:1403.1532
- Tamborra, I., Hüdepohl, L., Raffelt, G. G., & Janka, H.-T. 2017, *ApJ*, 839, 132
- Thielemann, F. K., Eichler, M., Panov, I. V., & Wehmeyer, B. 2017, *Annual Review of Nuclear and Particle Science*, 67, 253
- Tian, J. Y., Patwardhan, A. V., & Fuller, G. M. 2017, *Phys. Rev. D*, 96, 043001
- Vlasenko, A., Fuller, G. M., & Cirigliano, V. 2014, *PhRvD*, 89, 105004
- Volpe, C. 2015, *International Journal of Modern Physics E*, 24, 1541009
- Wanajo, S., Müller, B., Janka, H.-T., & Heger, A. 2018, *ApJ*, 852, 40
- Witt, M., Psaltis, A., Yasin, H., et al. 2021, arXiv e-prints, arXiv:2107.00687
- Wolfenstein, L. 1978, *PhRvD*, 17, 2369
- Wu, M.-R., & Tamborra, I. 2017, *Phys. Rev. D*, 95, 103007
- Wu, M.-R., Tamborra, I., Just, O., & Janka, H.-T. 2017, *Phys. Rev. D*, 96, 123015
- Zaizen, M., Cherry, J. F., Takiwaki, T., et al. 2020, *JCAP*, 2020, 011
- Zaizen, M., & Morinaga, T. 2021, arXiv e-prints, arXiv:2104.10532
- Zaizen, M., Yoshida, T., Sumiyoshi, K., & Umeda, H. 2018, *Phys. Rev. D*, 98, 103020